

Evolution of X-ray galaxy Cluster Properties in a Representative Sample (EXCPRoS)

Optimal binning for temperature profile extraction

C.M.H. Chen¹, M. Arnaud¹, E. Pointecouteau², G.W. Pratt¹, and A. Iqbal¹

¹ Université Paris-Saclay, Université Paris Cité, CEA, CNRS, AIM, 91191, Gif-sur-Yvette, France
e-mail: gabriel.pratt@cea.fr

² IRAP, Université de Toulouse, CNRS, CNES, UPS, 9 Av. colonel Roche, BP 44346, F-31028 Toulouse Cedex 4, France
e-mail: etienne.pointecouteau@irap.omp.eu

Received ; accepted

ABSTRACT

We present XMM-Newton observations of a representative X-ray selected sample of 31 galaxy clusters at moderate redshift ($0.4 < z < 0.6$), spanning the mass range $10^{14} < M_{500} < 10^{15} M_{\odot}$. This sample, EXCPRoS (Evolution of X-ray galaxy Cluster Properties in a Representative Sample), is used to test and validate a new method to produce optimally-binned cluster X-ray temperature profiles. The method uses a dynamic programming algorithm, based on partitioning of the soft-band X-ray surface brightness profile, to obtain a binning scheme that optimally fulfils a given signal-to-noise threshold criterion out to large radius. From the resulting optimally-binned EXCPRoS temperature profiles, and combining with those from the local REXCESS sample, we provide a generic scaling relation between the relative error on the temperature and the [0.3-2] keV surface brightness signal-to-noise ratio, and its dependence on temperature and redshift. We derive an average scaled 3D temperature profile for the sample. Comparing to the average scaled 3D temperature profiles from REXCESS, we find no evidence for evolution of the average profile shape within the redshift range that we probe.

Key words. galaxies: clusters: general – galaxies: clusters: intracluster medium – X-rays: galaxies: clusters

1. Introduction

Galaxy clusters form through the gravitational collapse of the dominant dark matter component, with the gas of the intra-cluster medium (ICM) ‘following’ the gravitational potential as the object grows by accretion and merging. The ICM is heated to X-ray emitting temperatures by shocks and compression during this hierarchical assembly process under gravity. Feedback from active galactic nuclei, supernovae, and gas cooling further modify the properties of the ICM over cosmic time (Kravtsov & Borgani 2012; Vogelsberger et al. 2014; Schaye et al. 2015, 2023).

In this context, spatially resolved measurements of the thermodynamic properties of the ICM contain crucial information on the physics governing the formation and evolution of groups and clusters. Radial profiles of gas density, n_e , and temperature, kT , have become fundamental tools for measurement of key quantities such as pressure, P , entropy, K , and hydrostatic mass, and for making comparisons with predictions from numerical simulations (see, e.g. Lovisari & Maughan 2022; Kay & Pratt 2022, for recent reviews). However, while the gas density is simple to obtain from X-ray imaging, determination of a radial temperature profile requires an annular binning scheme that yields sufficient signal to build and model the spectrum. The problem is compounded by the density-squared dependence of the X-ray emission, a typical cluster emissivity profile that steepens dramatically with radius, and by the drop in the signal-to-noise (S/N) at lower masses and higher redshifts.

The radial temperature profiles of local ($z \lesssim 0.3$) clusters and groups are now well characterised (Markevitch 1998; De Grandi & Molendi 2002; Vikhlinin et al. 2005, 2006; Pratt et al. 2007; Baldi et al. 2007; Leccardi & Molendi 2008; Sun et al. 2009; Arnaud et al. 2010; Lovisari et al. 2015). The temperature declines gradually towards the outer regions from a peak at $R \sim 0.2 R_{500}$. In the inner regions, non-cool core systems are typically approximately isothermal at the peak temperature, while cool core systems exhibit a characteristic smooth drop to $1/2 - 1/3$ of the peak temperature value. In particular, Vikhlinin et al. (2006) and Sun et al. (2009) showed the remarkable similarity and tight scaling with mass in relaxed systems. The Representative XMM-Newton Cluster Structure Survey (REXCESS), a representative sample of X-ray selected clusters, has provided the mean pressure profile, its dispersion, and the mass scaling (Arnaud et al. 2010) that is used in all matched multi-filter Sunyaev-Zeldovich effect (SZE) survey detection algorithms (e.g. Melin et al. 2006). It has also yielded strong constraints on the radial and mass dependence of the entropy distribution (Pratt et al. 2010).

Until recently however, individual radial temperature profiles were rarely available beyond $z > 0.3$ (however, see e.g. Kotov & Vikhlinin 2005; Baldi et al. 2012; Mantz et al. 2016 for pioneering studies). While the advent of SZE surveys by ACT (Hasselfield et al. 2013), SPT (Bleem et al. 2015) and Planck (Planck Collaboration XXVII 2016), has transformed the quest for high- z systems, X-ray follow-up deep enough to measure annular temperature profiles of these new $z > 0.3$ SZE-discovered clusters

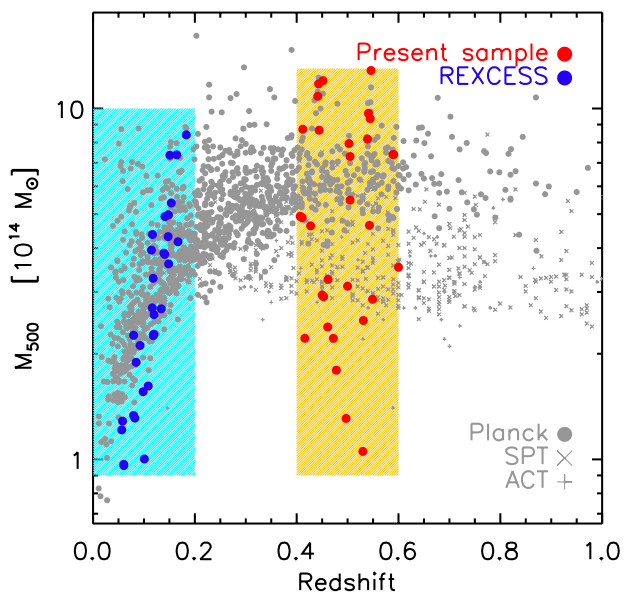


Fig. 1: Distribution in the $M - z$ plane of the EXCPReS sample (red points). The local X-ray-selected REXCESS sample (Böhlinger et al. 2007) is shown with blue points. Shown for comparison are confirmed clusters from major SZE surveys from which individual spatially resolved temperature profiles are measurable: Filled circles: *Planck* clusters (Planck Collaboration VIII 2011; Planck Collaboration XXIX 2014; Planck Collaboration XXVII 2016). Crosses: SPT (Bleem et al. 2015). Plus symbols: ACT (Hasselfield et al. 2013).

has concentrated on the highest-mass objects. Being X-ray bright, they are the ‘easiest’ systems to observe, leading to good a precision on the radial temperature distribution (see e.g. Bartalucci et al. 2017, 2019, where the individual thermodynamic profiles of systems up to $z \sim 1$ are measured). Results from stacking (e.g. McDonald et al. 2014) can yield the average behaviour, but do not offer insights into the intrinsic scatter in the profiles.

In this paper we introduce the Evolution of X-ray galaxy Cluster Properties in a Representative Sample (EXCPReS). Consisting of 31 X-ray-selected clusters in the redshift range $0.4 < z < 0.6$ and the mass range $0.1 - 1.3 \times 10^{15} M_{\odot}$, EXCPReS was designed to be a moderate-redshift analogue of REXCESS. We use EXCPReS to test and validate a novel method to optimally bin X-ray data to reconstruct the 3D temperature distribution of the ICM. In the following, we present the EXCPReS sample, the XMM-Newton observations and data analysis. We describe our method for binning of the surface brightness profiles to derive optimal temperature profiles. The method is applied to the EXCPReS sample, and the resulting profiles, and their dispersion, are compared to those of the local REXCESS sample. Throughout this paper we assume a flat Λ CDM model with $H_0 = 70 \text{ km s}^{-1} \text{ Mpc}^{-1}$, $\Omega_m = 0.3$ and $\Omega_{\Lambda} = 0.7$. Uncertainties are quoted at the 68% confidence level. The variables M_{500} and R_{500} are the total mass within R_{500} and radius corresponding to a total density contrast of $\Delta = 500 \rho_c(z)$, where $\rho_c(z)$ is the critical density of the universe at the cluster redshift.

2. The sample

Our aim is to obtain spatially-resolved temperature measurements at moderate redshift across the full cluster mass range (i.e. $M_{500} \gtrsim 10^{14} M_{\odot}$). As SZE-selected clusters typically probe higher masses (see Fig. 1), we chose to focus instead on X-ray selected clusters at a median redshift of $z = 0.5$. A logical local reference in this case

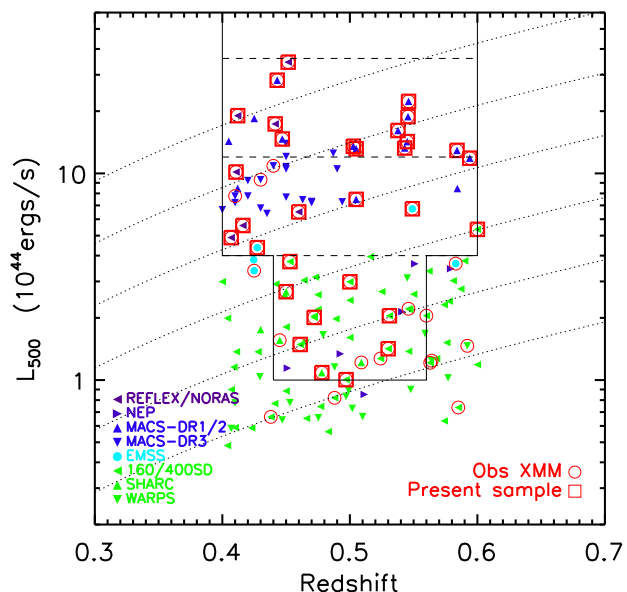


Fig. 2: Distribution of the MCXC clusters in the $z-L_{500}$ plane (Piffaretti et al. 2011). Redshift and L_{500} , the luminosity within R_{500} , are from the updated MCXC catalogue (Sadibekova et al. 2023). Each cluster is colour-coded according to the survey from which the luminosity is taken. Clusters with XMM-Newton observations are marked with red circles and those included in the EXCPReS sample are marked with red boxes. The dotted lines mark the $[0.1-2.4] \text{ keV}$ band flux taking into account the K_z correction for a typical gas temperature of 5 keV. Levels are separated by 2 dex, from 1.25×10^{-13} up to $4 \times 10^{-12} \text{ ergs s}^{-1} \text{ cm}^{-2}$.

is the REXCESS sample (Böhlinger et al. 2007), which covers a similar mass range, but at lower redshifts ($0.055 < z < 0.183$). The chosen median redshift of EXCPReS is the highest z for which we can define a complete sample covering the whole cluster mass range of the various ROSAT surveys. Indeed, clusters below $\sim 10^{14} M_{\odot}$ have such low luminosities that at $z \gtrsim 0.6$ they begin to fall rapidly below the detection limits of these surveys.

2.1. Parent MCXC sample

Our sample is drawn from the Meta Catalogue of X-ray detected Clusters of galaxies (MCXC; Piffaretti et al. 2011). MCXC is based on the Einstein Medium Sensitivity Survey (EMSS Gioia et al. 1990; Henry 2004) and on the ROSAT All-Sky and Serendipitous surveys. We used the MCXC-II, which includes updated redshifts and ~ 500 additional clusters (Sadibekova et al. 2024). Redshift revision was based on comparison of the redshifts from the NED and Simbad data bases, and cross-matching with cluster catalogues extracted from large optical surveys, in particular the SDSS (e.g. Wen & Han 2015; Rykoff et al. 2016).

The distribution in the $L_{500}-z$ plane of the 134 MCXC-II clusters with $0.4 < z < 0.6$ is shown in Fig. 2. Different flux levels are indicated by dotted lines. These trace the $[0.1-2.4] \text{ keV}$ band flux, taking into account the K_z correction for a typical gas temperature of 5 keV. The five levels are separated by 2 dex, from 1.25×10^{-13} up to $4 \times 10^{-12} \text{ ergs s}^{-1} \text{ cm}^{-2}$. Surveys are distinguished by different symbols and colours. For clusters appearing in several catalogues (i.e. detected in different surveys), we only indicate the input catalogue used to compute the luminosity, following the MCXC-II hierarchy described in Sadibekova et al. (2024).

The sub-samples of clusters from the ROSAT All-Sky survey (RASS) and the Serendipitous surveys appear quasi disjointed in the redshift range under consideration. There are 43 RASS clus-

Table 1: EXCPReS sample and XMM-Newton observations. Columns are 1: object index. 2-5: Cluster MCXC name, other name, detection survey and redshift. 6-7: Right ascension and declination in 2000 equinox of X-ray peak in XMM-Newton image. 6: XMM-Newton OBSID. 7: EPIC (total EMOS and EPN) effective exposure time (i.e. after flare cleaning).

ID	Name	Other Name	Catalogue	z	RA (h,m,s)	DEC (d,am,as)	OBSID	Exp. MOS/PN ksec
1	MCXC J0018.5+1626	MACS J0018.5+1626; CL 0016+1609	MACS; EMSS	0.541	0 18 33	+16 26 08	0111000101 0111000201	33.3/23.9
2	MCXC J0030.5+2618	[BVH2007] 2; [VMF98] 1	400SD; WARPSII; 160SD	0.500	0 30 33	+26 18 06	0402750201	26.9/ 19.7
3	MCXC J0221.1+1958	RX J0221.1+1958	SHARC BRIGHT	0.450	2 21 09	+19 58 03	0402750301	25.8/ 16.0
4	MCXC J0257.1-2326	MACS J0257.1-2325	MACS	0.505	2 57 08	-23 26 07	0551850201	25.6/ 9.9
5	MCXC J0417.5-1154	MACS J0417.5-1154	MACS	0.443	4 17 34	-11 54 32	0827310101	9.9/ 4.7
6	MCXC J0454.1-0300	MACS J0454.1-0300; MS 0451.6+0305	MACS; EMSS	0.539	4 54 10	-03 00 57	0205670101	22.0/17.2
7	MCXC J0522.2-3624	[VMF98] 41	400SD ;160SD	0.472	5 22 15	-36 25 11	0302580901	18.2/14.4
8	MCXC J0647.8+7014	MACS J0647.7+7015	MACS	0.591	6 47 50	+70 14 53	0551850401 0551851301	71.4/44.6
9	MCXC J0717.5+3745	MACS J0717.5+3745	MACS	0.546	7 17 31	+37 45 31	0672420101 0672420201 0672420301	156.5/116.5
10	MCXC J0856.1+3756	RXC J0856.1+3756	NORAS	0.411	8 56 12	+37 56 09	0302581801	18.3/ 6.6
11	MCXC J0911.1+1746	MACS J0911.2+1746	MACS	0.505	9 11 11	+17 46 33	0693662501	33.0/25.5
12	MCXC J0943.1+4659	RXC J0943.1+4659; A0851	NORAS	0.407	9 43 00	+46 59 28	0106460101	32.4/20.7
13	MCXC J0957.8+6534	RXC J0957.8+6534	160SD	0.530	9 57 51	+65 34 24	0502430201	37.4/22.0
14	MCXC J1003.0+3254	RXC J1003.0+3254	NORAS; 400SD	0.416	10 03 04	+32 53 44	0302581601	22.2/ 7.2
15	MCXC J1120.1+4318	RX J1120.1+4318	400SD; SHARC BRIGHT; WARPSII	0.600	11 20 07	+43 18 07	0107860201	17.7/10.7
16	MCXC J1149.5+2224	MACS J1149.5+2223	MACS; NORAS	0.544	11 49 35	+22 24 03	0693661701	12.5/ 2.1
17	MCXC J1206.2-0848	RXC J1206.2-0848	REFLEX; MACS	0.441	12 06 12	-08 48 00	0502430401	29.1/21.0
18	MCXC J1244.0+1653	MS1241.5+1710	EMSS	0.549	12 44 01	+16 53 43	0302581501	28.7/19.0
19	MCXC J1311.5-0551	RX J1311.5-0551	160SD	0.461	13 11 30	-05 52 03	0302582201	21.4/17.0
20	MCXC J1347.5-1144	RX J1347.5-1145	REFLEX; MACS	0.452	13 47 30	-11 45 08	0112960101	32.3/25.4
21	MCXC J1411.4+5212	RXC J1411.4+5212 3C295	NORAS	0.462	14 11 20	+52 12 10	0804271501	15.3/12.2
22	MCXC J1423.7+2404	MACS J1423.8+2404	MACS	0.543	14 23 48	+24 04 43	0720700401	23.1/19.4
23	MCXC J1623.5+2634	MS1621.5+2640	EMSS	0.427	16 23 35	+26 34 20	0112190701	4.3/0.0
24	MCXC J1701.3+6414	RXC J1701.3+6414	400SD; SHARC BRIGHT; 160SD	0.453	17 01 23	+64 14 09	0723700201	35.3/30.5
25	MCXC J2129.4-0741	MACS J2129.4-0741	MACS	0.589	21 29 26	-07 41 28	0700182001	8.6/3.3
26	MCXC J2146.0+0423	RX J2146.0+0423	160SD; WARPS	0.531	21 46 05	+04 23 00	0302580701	20.7/17.2
27	MCXC J2214.9-1400	MACS J2214.9-1359	MACS	0.503	22 14 57	-14 00 16	0693661901	17.4/ 7.1
28	MCXC J2228.6+2036	RXC J2228.6+2036	NORAS; eBCS	0.412	22 28 33	+20 37 13	0147890101	23.2/14.6
29	MCXC J2243.3-0935	MACS J2243.3-0935	MACS	0.444	22 43 21	-09 35 40	0503490201	102.9/77.2
30	MCXC J2328.8+1453	RX J2328.8+1453	160SD; WARPSII	0.497	23 28 51	+14 53 01	0502430301	85.7/62.9
31	MCXC J2359.5-3211	RX J2359.5-3211	SHARC SOUTH	0.478	23 59 36	-32 11 17	0302580501	36.3/19.6

ters above a luminosity of 4×10^{44} ergs s^{-1} (flux above $\approx 10^{-12}$ ergs $s^{-1} cm^2$), from the NORAS (Böhringer et al. 2000), REFLEX (Böhringer et al. 2004) and/or MACS catalogues. Following the MCXC-II nomenclature, the latter include the MACS-DR1 sample of the highest- z ($z > 0.5$) clusters (Ebeling et al. 2007), the DR2 flux-limited sample of the brightest $0.3 < z < 0.5$ MACS clusters (Ebeling et al. 2010) and the deeper MACS-DR3 catalogue (Mann & Ebeling 2012, excluding overlap with DR1 and DR2)¹. Only six RASS clusters lie below 4×10^{44} ergs s^{-1} , which are clusters from the North Ecliptic Pole (NEP) deeper part of the All-sky survey (Henry et al. 2006). In contrast, all 80 clusters from ROSAT Serendipitous surveys lie at $L_{500} < 10^{44}$ ergs s^{-1} , with the exception of RXJ 1120.1+4318 at $z=0.6$ (Romer et al. 2000). These come from the 160SD (Vikhlinin et al. 1998; Mullis et al. 2003), 400SD (Burenin et al. 2007), B-SHARC (Romer et al. 2000), S-SHARC (Burke et al. 2003), WARPS-I (Perlman et al. 2002) and WARPS-II (Horner et al. 2008) catalogues.

Finally there are five EMSS (Gioia et al. 1990; Henry 2004) clusters that were not rediscovered in the subsequent ROSAT surveys, three at luminosity below 4×10^{44} ergs s^{-1} and two above. The two other EMSS clusters in the redshift range are the luminous clusters MCXC J0018.5+1626 (CL0016+16 at $z =$

0.55) and MCXC J0454.1-0300 ($z = 0.54$), rediscovered in the MACS survey. Hereafter, the high- L_X and low- L_X subsamples include clusters above and below a luminosity of 4×10^{44} ergs s^{-1} , respectively.

2.2. EXCPReS sample

We searched for XMM-Newton observations, with pointing position within $5'$ of the cluster centre, available by September 2021 in the ESA archive². The observed clusters are marked with red circles in Fig. 2 and those selected to form the EXCPReS sample are marked with red boxes.

The core of the EXCPReS sample is the XMM-Newton Large-Programme follow-up of EMSS, NORAS, REFLEX, B-SHARC, S-SHARC, 160SD and WARPS-I samples (programme ID #030258 with re-observation of flared observations in ID #040275 and #050243, combined with previous archival data). It was designed to study evolution from comparison with REXCESS data, similarly constructing a representative sample of clusters centered at a median redshift of $z = 0.5$ with homogenous coverage of the luminosity space (Arnaud 2008). The redshift excursion below $L_{500} \sim 4 \times 10^{44}$ ergs s^{-1} was set to $0.45 < z < 0.55$ and increased to $0.4 < z < 0.6$ to include all the rare high z massive clusters known at that time. Additional observations essentially extend the high luminosity coverage, mostly thanks to the publication of MACS clusters and corresponding follow-up.

² <https://www.cosmos.esa.int/web/xmm-newton/xsa>

¹ MCXC-II also includes additional MACS clusters recovered from non-catalogue studies (the MACS_MISC sub-catalogue). We discarded them in this study as their X-ray selection function is not defined. In the redshift range under consideration, this concerns four clusters from the on-going extension of the MACS survey in the South (Repp & Ebeling 2018).

Table 2: Physical parameters of the sample. Columns 1-3: Cluster index, MCXC name and redshift. 4: Hydrogen column density from the LAB survey 21 cm measurements (Kalberla et al. 2005). Columns 5-6: M_{500} is the mass within R_{500} , the radius enclosing 500 times the critical density at the cluster redshift. T_X is the temperature measured in the $[0.15-0.75] R_{500}$ aperture. M_{500} and T_X are measured iteratively using the $M_{500}-Y_X$ relation (Arnaud et al. 2007) assuming self-similar evolution, where Y_X is the product of T_X and the gas mass within R_{500} . 7-8: Count rate in the $[0.3 - 2]$ keV energy band within an aperture of R_{500} in radius, and corresponding signal-to-noise (S/N) ratio.

Obs.	Name	z	N_{H} 10^{20} cm^{-2}	T_X keV	M_{500} $10^{14} M_{\odot}$	CR_{500} ct/s	S/N ₅₀₀
1	MCXC J0018.5+1626	0.541	3.99	9.66 ± 0.33	9.69 ± 0.23	1.17	149
2	MCXC J0030.5+2618	0.500	3.71	5.40 ± 0.42	3.12 ± 0.18	0.20	47
3	MCXC J0221.1+1958	0.450	9.12	5.44 ± 0.41	2.94 ± 0.16	0.24	50
4	MCXC J0257.1-2326	0.505	2.08	8.32 ± 0.40	7.30 ± 0.24	1.10	102
5	MCXC J0417.5-1154	0.443	3.32	9.01 ± 0.36	11.75 ± 0.45	3.29	117
6	MCXC J0454.1-0300	0.539	3.92	9.06 ± 0.32	8.18 ± 0.20	1.13	122
7	MCXC J0522.2-3624	0.472	3.63	4.25 ± 0.42	2.21 ± 0.17	0.16	34
8	MCXC J0647.8+7014	0.591	8.53	8.03 ± 0.19	7.39 ± 0.12	0.79	156
9	MCXC J0717.5+3745	0.546	6.63	10.30 ± 0.15	12.83 ± 0.17	1.53	359
10	MCXC J0856.1+3756	0.411	3.21	6.20 ± 0.42	4.89 ± 0.24	0.59	54
11	MCXC J0911.1+1746	0.505	3.28	6.70 ± 0.28	5.48 ± 0.22	0.55	99
12	MCXC J0943.1+4659	0.407	1.00	5.53 ± 0.17	4.93 ± 0.11	0.70	100
13	MCXC J0957.8+6534	0.530	5.33	2.86 ± 0.31	1.05 ± 0.08	0.07	31
14	MCXC J1003.0+3254	0.416	1.68	3.71 ± 0.25	2.21 ± 0.11	0.35	40
15	MCXC J1120.1+4318	0.600	2.97	5.00 ± 0.32	3.53 ± 0.15	0.35	54
16	MCXC J1149.5+2224	0.544	1.92	8.79 ± 0.60	9.36 ± 0.63	1.14	47
17	MCXC J1206.2-0848	0.441	4.35	10.15 ± 0.32	10.83 ± 0.25	2.34	203
18	MCXC J1244.0+1653	0.549	1.77	4.60 ± 0.24	2.86 ± 0.12	0.48	85
19	MCXC J1311.5-0551	0.461	2.43	5.69 ± 0.99	2.38 ± 0.28	0.09	23
20	MCXC J1347.5-1144	0.452	4.60	11.74 ± 0.25	12.01 ± 0.17	4.80	327
21	MCXC J1411.4+5212	0.462	1.32	4.88 ± 0.33	3.26 ± 0.23	0.81	86
22	MCXC J1423.7+2404	0.543	2.20	5.90 ± 0.25	4.64 ± 0.18	1.01	128
23	MCXC J1623.5+2634	0.427	3.12	5.73 ± 0.96	4.63 ± 0.59	0.21	24
24	MCXC J1701.3+6414	0.453	2.28	4.00 ± 0.19	2.91 ± 0.13	0.37	66
25	MCXC J2129.4-0741	0.589	4.32	8.28 ± 0.79	7.39 ± 0.66	0.77	47
26	MCXC J2146.0+0423	0.531	4.82	5.16 ± 0.59	2.49 ± 0.20	0.13	31
27	MCXC J2214.9-1400	0.503	2.88	8.19 ± 0.48	7.95 ± 0.44	1.17	83
28	MCXC J2228.6+2036	0.412	4.26	8.16 ± 0.30	8.73 ± 0.23	1.66	133
29	MCXC J2243.3-0935	0.444	4.02	7.44 ± 0.09	8.67 ± 0.10	1.69	302
30	MCXC J2328.8+1453	0.497	3.88	3.17 ± 0.25	1.31 ± 0.08	0.05	38
31	MCXC J2359.5-3211	0.478	1.18	3.57 ± 0.33	1.79 ± 0.12	0.13	37

The high- L_X subsample has good XMM-Newton follow-up coverage. The EMSS and REFLEX/NORAS clusters have all been observed with deep XMM-Newton pointings (nine clusters), as well as the only cluster from a ROSAT serendipitous survey (a B-SHARC object). The XMM-Newton follow-up of the MACS clusters depends on the sub-catalogues. The XMM-Newton follow-up of the MACS-DR1 and MACS-DR2 clusters is nearly complete, with twelve clusters observed. Only one MACS-DR1 cluster (MCXC J0025.4-1222 at $z = 0.584$) and three DR2 clusters (MACS J0152.5-2852, MACS J0159.8-0849, MACS J0358.8-2955) are lacking observations. In contrast, only three of the seventeen DR3 clusters have been observed. We decided to discard these three observations and to include the remaining 22 clusters observed by XMM-Newton. In this way, above a luminosity of $4 \times 10^{44} \text{ ergs s}^{-1}$, our sample constitutes a nearly complete follow-up, with a completion factor of 22/26 or 85%, of cluster catalogues (EMSS, NORAS/REFLEX, MACS-DR1/DR2 and B-SHARC), with a well defined selection function.

The XMM-Newton follow-up at lower luminosity is more sparse. Beyond the objects of the LP observations mentioned above, no archival observations are deep enough to allow anything

but a global temperature measurement to be obtained. This is discussed in more detail in Appendix A. The final selection at low luminosity includes nine clusters in the $0.44 < z < 0.56$ redshift range with $L_{500} > 10^{44} \text{ ergs s}^{-1}$. In this redshift range, four objects with archival XMM-Newton data are not included: one is actually a point source, and three are SHARC clusters with insufficiently deep observations.

The final EXCPReS sample comprises 31 clusters in three boxes in the $L_{500}-z$ plane (see Fig. 2), centred at a redshift of $z = 0.5$, with an approximately equal number of clusters in three equal logarithmically spaced luminosity bins. There are nine clusters in the low-luminosity bin $10^{44} < L_{500} < 4 \times 10^{44} \text{ ergs s}^{-1}$, nine clusters at intermediate luminosity, $4 \times 10^{44} < L_{500} < 12 \times 10^{44} \text{ ergs s}^{-1}$, and thirteen in the high luminosity bin, $12 \times 10^{44} < L_{500} < 36 \times 10^{44} \text{ ergs s}^{-1}$.

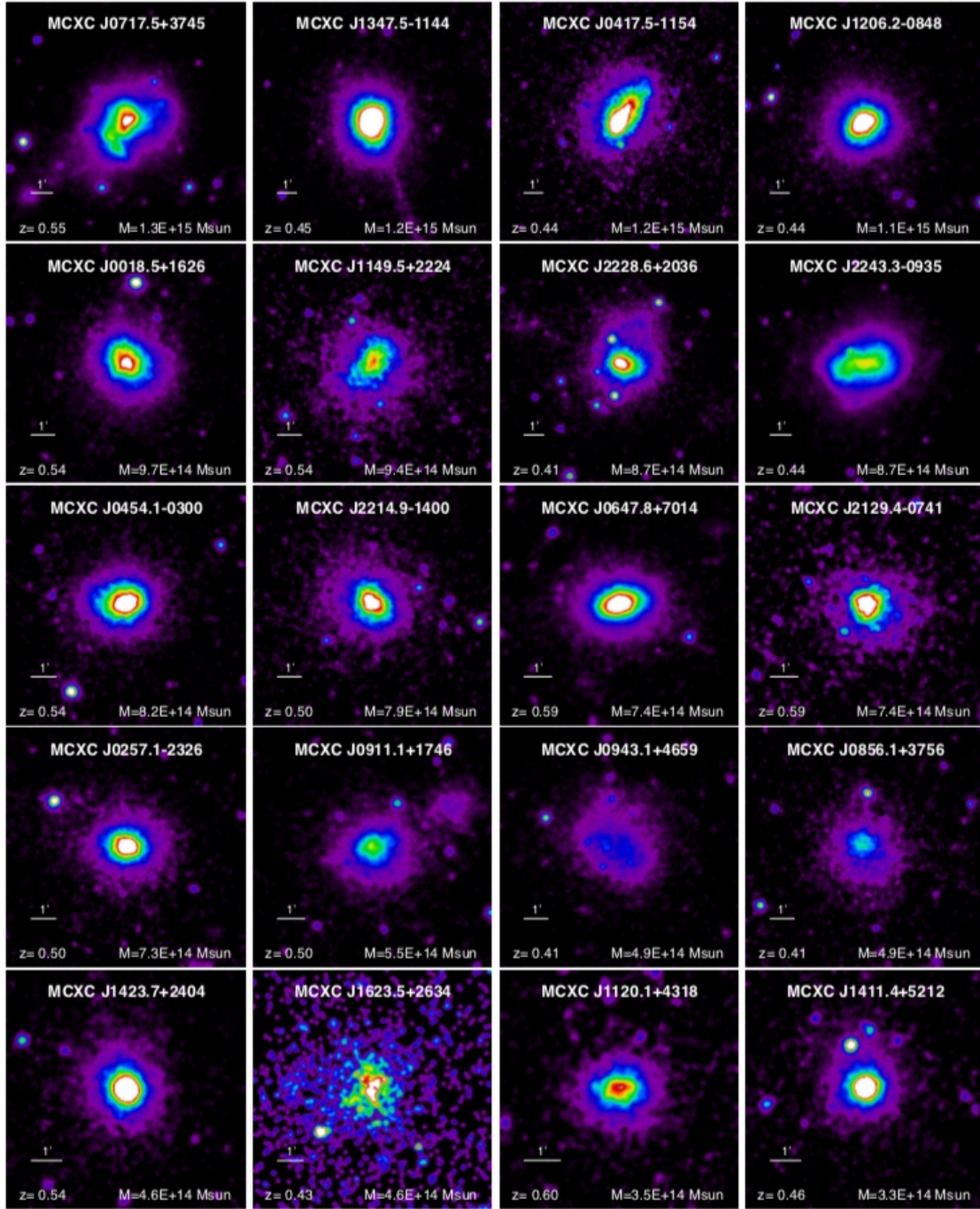


Fig. 3: Gallery of the XMM-Newton images, extracted in the [0.3–2] keV energy band, for the 31 clusters of the sample, ordered by decreasing mass. Image sizes are $3\theta_{500}$ on a side, where θ_{500} is estimated from the $M_{500}-Y_X$ relation. Images are corrected for surface brightness dimming with z , divided by the emissivity in the energy band, taking into account galactic absorption and instrument response, and scaled according to the self-similar model. The colour table is the same for all clusters, so that the images would be identical if clusters obeyed self-similarity.

3. XMM-Newton observations and data processing

3.1. Data preparation

All data sets were retrieved and reprocessed with the XMM-Newton Science Analysis Software, using the methods described extensively in for instance Bartalucci et al. (2017). In brief, the events list were (i) cleaned for solar flare contamination (Pratt & Arnaud 2003); (ii) filtered with PATTERN-selected (0-12 for EMOS and 0-4 for EPN); (iii) corrected for vignetting (by attributing a vignetting weight function to each event, see Arnaud et al.

2001); (iv) point source subtracted (after detection in the [0.3–2] keV and [2–5] keV co-added EMOS+EPN image using the SAS task ewavedetect, tuned to a detection threshold of 5σ and double-checked visually). All clusters have effective observation from the three XMM-Newton cameras, except MS1621.5+2640 whose PN data had to be discarded due to a high rate of contamination by solar flares. Table 1 lists the observation details for the sample. Exposure times are the sum of EMOS (EMOS1 and EMOS2) and the EPN effective exposure time (i.e. after flare cleaning).

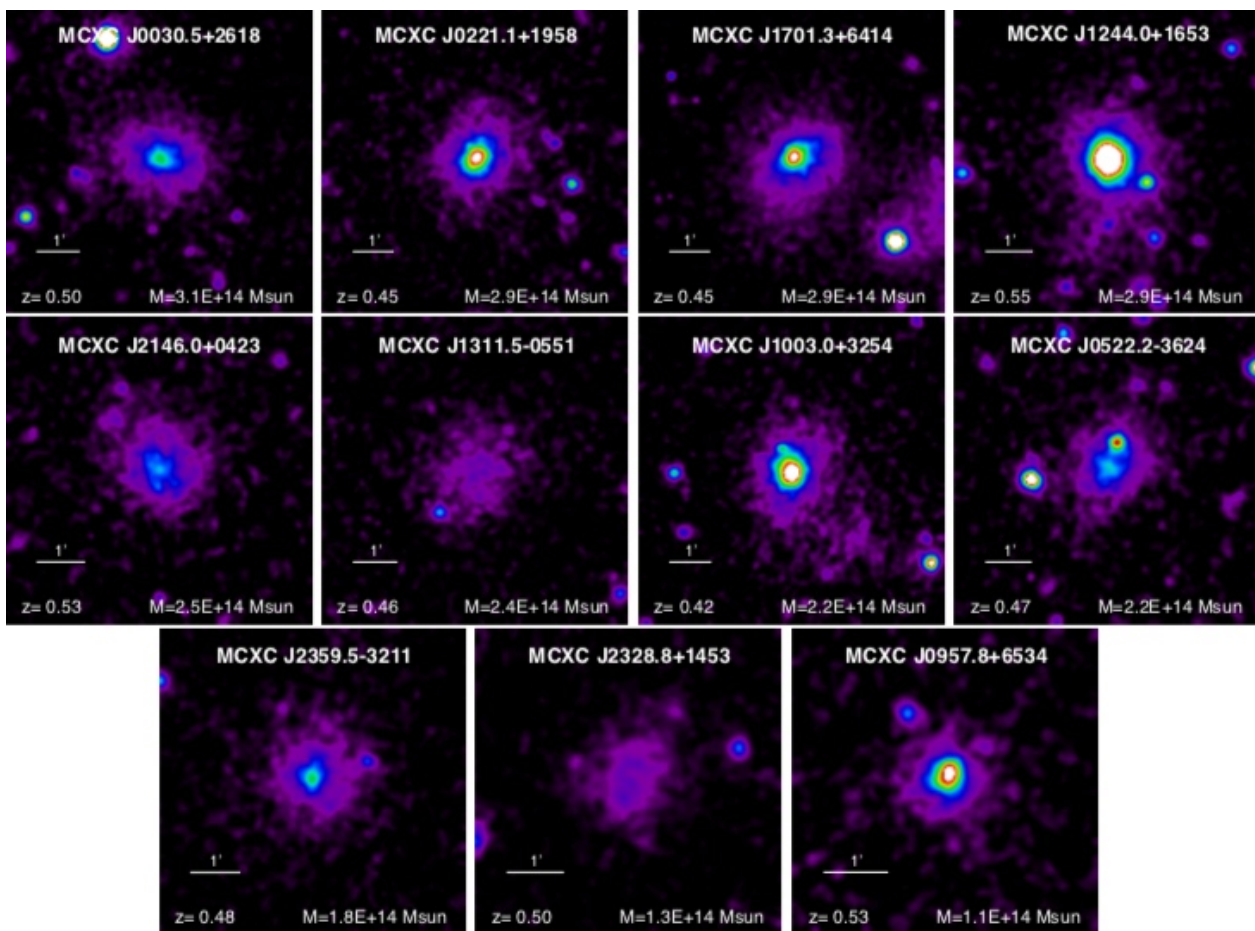


Fig. 4: Gallery of X-ray images for the clusters of the sample, continued.

The (solar) particle plus instrumental background templates used in later spatial and spectral analysis were obtained by stacking Filter Wheel Closed (FWC) observations for each camera. The same cleaning, PATTERN selection and vignetting correction steps were applied to the FWC events lists. The FWC files were finally cast to match the astrometry of each cluster observation and renormalised to the quiescent count rate in the [10-12] and [12-14] keV bands for EMOS and EPN, respectively.

3.2. Imagery and spectral analysis

Images and surface brightness (S_X) profiles were extracted in the [0.3 – 2.0] keV band in order to maximise the S/N. The S_X data points were defined in fixed circular radial bins of $3''3$ width, hence assuming spherical symmetry.

Spectral analysis followed that described extensively in Pratt et al. (2010) and Bartalucci et al. (2017). Spectra were extracted in various regions of interest from the weighted events lists. The instrumental background was subtracted using the FWC spectrum from the same region in detector coordinates, normalised in the high-energy band. The cosmic X-ray background was obtained from modelling an FWC-subtracted region external to the cluster emission, normalised in the high energy band (accounting for chip gaps, missing pixels, etc)³. The model used was the sum of an unabsorbed thermal model (local bubble) added to the absorbed sum of a thermal (Galactic halo) and power law (CXB) models. It is considered constant across the cluster area and

geometrically scaled in normalisation to each annulus in the modelling step. The cluster spectra were fitted with an absorbed redshifted thermal model (mekal under XSPEC), together with the CXB model above, scaled to the area of the extraction region. Fits were undertaken in the [0.3 – 10] keV band. The spectrum from the $[0.15 - 0.75] R_{500}$ region was fitted with the n_H free and the result was compared to the standard Leiden/Argentine/Bonn (LAB; Kalberla et al. 2005) 21 cm survey value. In no cases was the fitted n_H significantly different from the LAB result, so this value was used.

3.3. Global cluster properties

The values for M_{500} and the corresponding R_{500} were computed iteratively from the $M_{500}-Y_X$ relation, calibrated by Arnaud et al. (2007) using HE mass estimates of local relaxed clusters. We assumed that the $M_{500}-Y_X$ relation obeys self-similar evolution. The quantity Y_X is defined as the product of the temperature T_X measured in the $[0.15-0.75] R_{500}$ region and the gas mass within R_{500} (Kravtsov et al. 2006). The gas masses were computed from the density profiles, derived from non-parametric deprojection of surface brightness profiles and the emissivity profile computed from the 2D temperature profile, as described in Croston et al. (2006). The temperature T_X and mass M_{500} for each cluster and associated errors are reported in Table 2. The table also lists the total count rate in the [0.3 – 2.0] keV band within an aperture of R_{500} in radius, and the total S/N within the R_{500} aperture.

³ Typical cluster angular radii, R_{500} , at these z are $\lesssim 5'$.

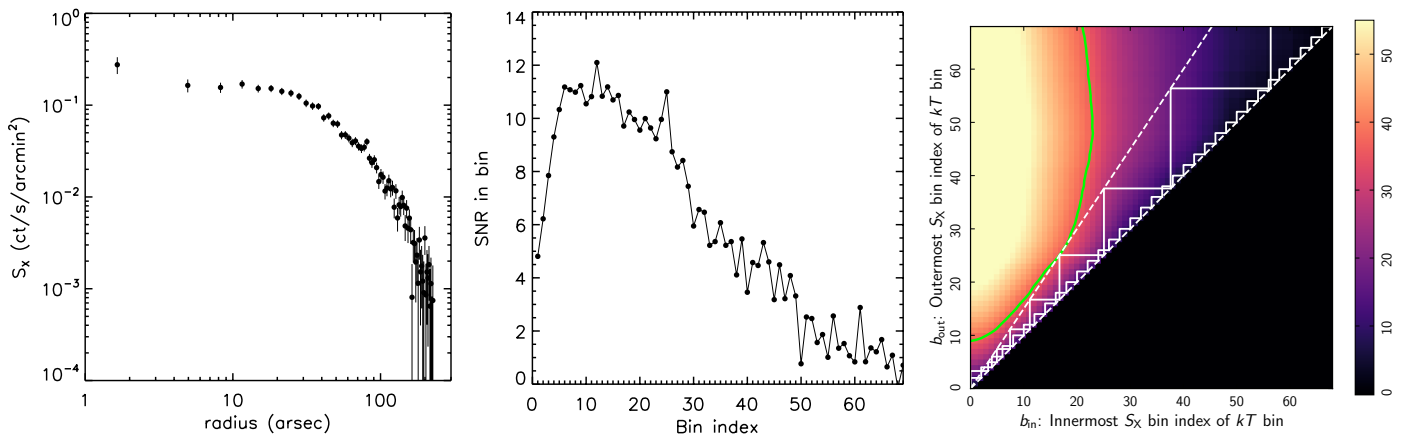


Fig. 5: Visual representation of the problem of binning surface-brightness (S_X) bins into temperature-profile (kT) bins. *Left*: S_X profile of RXJ0856.1+3756 in the [0.3-2] keV band, extracted in $3'' \times 3$ circular radial bins. *Centre*: Signal-to-noise ratio (S/N) in each bin of the S_X profile as a function of the bin index. *Right*: Innermost vs outermost S_X bin indexes, overplotted on the S/N obtained from placing the range of S_X bins indicated by the axes into one single kT bin. The green line delineates a 30σ S/N requirement. Two S_X example binning schemes are also shown (solid step curves). These correspond to a fixed binning of two input S_X bins (small fixed width steps), and a logarithmic binning of the S_X profile (continuously increasing step size).

Figure 1 shows the distribution of the EXCPRoS clusters in the z - M_{500} plane. It confirms that the sample covers a similar mass range to REXCESS with good mass sampling. However, EXCPRoS extends to slightly higher masses. Four objects have masses $M_{500} > 10^{15} M_{\odot}$, which is 20% larger than the maximum mass of the REXCESS sample, which is limited by the local Universe volume.

3.4. Images

We computed images in the [0.3-2.0] keV energy band in order to maximize the S/N. The images, for each available detector, were generated from the flare cleaned events lists, before point source subtraction, but corrected from the vignetting effect (with the SAS task `evweight`). They have been excised individually for bad pixels and detector gaps, and then co-added. A count image was extracted from the EPN out-of-time events lists and subtracted from the EPN count image.

An effective exposure time image was obtained from the sum of individual detector exposure maps (outputs of SAS task `eexmap` without vignetting correction), weighted by the relative efficiency of each detector in the [0.3-2.0] keV band. The total count image is then divided by this exposure map and then corrected for surface brightness dimming with z , divided by the EPIC emissivity in the energy band, taking into account galactic absorption and EPIC instrument response. This final image is a map of the emission measure along the line of sight. It is then scaled according to the standard self-similar model ($EM \propto R_{500} h(z)^2$), so that all images would be identical for a perfect self-similar model.

The gallery of images for our 31 clusters is shown in Figs. 3 and 4, ordered by decreasing mass. They are displayed with a linear scale. It can be seen that the clusters cover a wide range of luminosity and morphologies.

4. An optimal temperature profile binning method

Temperature profile binning is commonly undertaken by simply imposing a fixed bin width, or by applying some mathematical first-principle closed-form function (e.g. logarithmic binning), or by sizing the bins to obtain a given total number of counts in a

given energy band. These solutions can lead to a suboptimal use of the data set by not accounting for the underlying signal and noise distributions. To exploit the spatial resolution of the instrument to its maximum, so that surface-brightness (S_X) binning will yield sufficient counts per kT bin to build and model a spectrum, in the following, we describe an optimal binning algorithm based on the well-known combinatorial-optimisation algorithm ‘dynamic programming’ (Art & Mauch 2007; Cormen et al. 2009).

4.1. Problem description

The left-hand panel of Fig. 5 shows the [0.3-2] keV surface brightness profile of RX J0856.1+3756 extracted in circular $3'' \times 3$ radial bins. This bin width was chosen as it is an integer multiple (3) of the XMM-Newton EPIC pn pixel size, and therefore maximises the angular resolution of the resulting S_X profile in view of the mirror point spread function. The middle panel of Fig. 5 shows the resulting S/N of each S_X bin as a function of bin index. The S/N is simply defined as the ratio of the S_X to its statistical error, corresponding to $S/N = \sqrt{N}$ in a pure Poisson regime, where N is the number of counts in a given bin. In our case the statistical uncertainties include the errors added in quadrature from subtraction of the instrumental (CLOSED) and astrophysical local backgrounds (see e.g. Bartalucci et al. 2017). The S/N profile exhibits a typical behaviour where the S/N rises sharply to a peak in the inner regions, before tapering off quasi-linearly with increasing bin index. Each individual S/N is clearly insufficient to build a spectrum, hence the need for a specific rebinning of the S_X profile in order to extract the temperature profile.

The right-hand panel of Fig. 5 illustrates the binning problem visually. With the input S_X bins labelled with increasing numbers outwards, the x-axis indicates the innermost S_X bin of an output kT bin, while the y-axis indicates the outermost S_X bin. The underlying colour image indicates the S/N obtained from placing the range of S_X bins indicated by the axes into one single kT bin⁴.

A binning solution (a ‘partition’ hereafter) is then a set of adjacent kT bins that cover the entire range of S_X bins. In Fig. 5,

⁴ The bottom-right triangular half of the figure where $innermost S_X bin > outermost S_X bin$ is, obviously, to be disregarded.

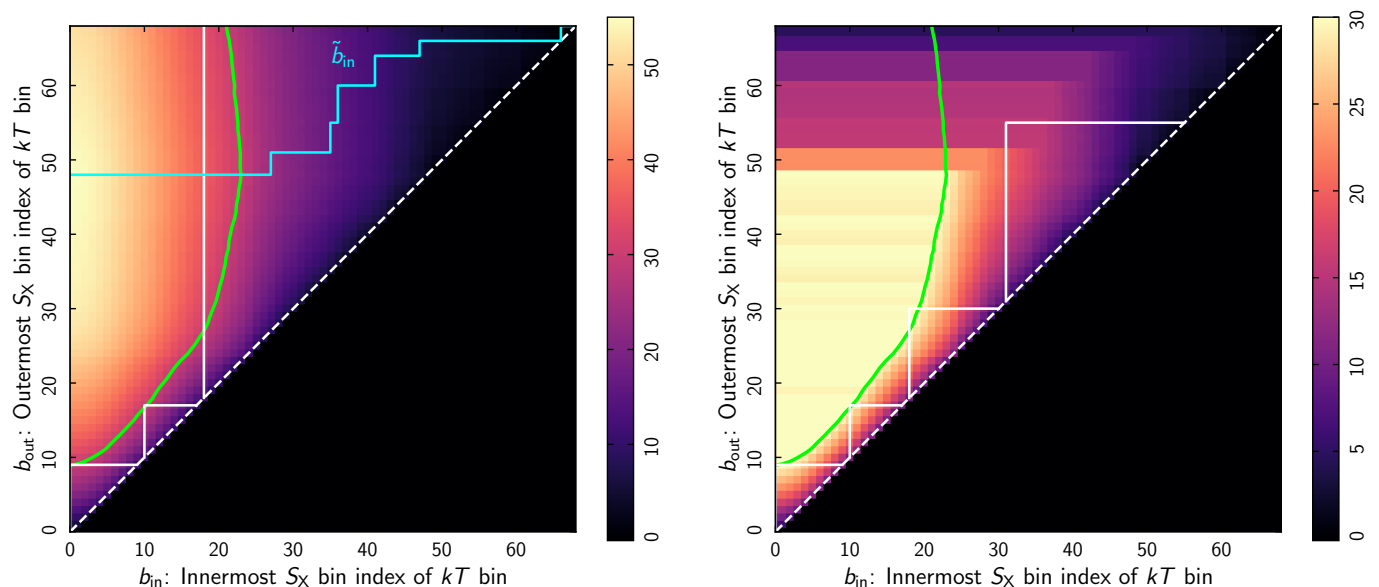


Fig. 6: Example binning solutions. *Left*: Initial binning solution for the galaxy cluster RXJ0856.1+3756 (solid white steps) from the algorithm specified in Sect. 4.3. The solid green curve delineates a 30σ S/N requirement. It shows that indefinitely adding more input S_X bins to an output kT bin is suboptimal. The cyan steps represent \tilde{b}_{in} , corresponding to the optimal innermost S_X bin to include per kT bin, described in the galaxy-cluster specific amendment in Sect. 4.3.2. *Right*: Same but with the galaxy-cluster specific amendment applied. Here, the S/N landscape is capped (1) globally to the S/N value at the rightmost b_{in} above 30σ for each b_{out} , and (2) at $b_{in} < \tilde{b}_{in}$ to the S/N value at \tilde{b}_{in} for each b_{out} . The colour scheme has been adjusted so that the effect of the S/N landscape capping procedure is visible.

a partition is represented as a contiguous set of steps starting at $(0, 0)$ and ending at the top-right corner. A step running from innermost S_X bin a to outermost S_X bin b represents an output kT bin covering input S_X bins from a to b .

Figure 5 illustrates two possible partitions. The first is a partition defined by mapping two S_X bin into one kT bin, which is represented as a series of two S_X -bin tall steps running along the diagonal. The second is a logarithmic binning solution, which results in steps whose vertices lie along some straight line starting from the origin and having slope > 1 . From such a visualisation, we would like to solve the binning problem in a data-driven way by defining a partition scheme accounting for the expected S/N level. That is, we would like the bin vertices to lie on coloured pixels having as high S/N as possible.

4.2. Definition of optimal binning

What does it mean to bin optimally? In our case, optimal binning (for temperature profile measurement) is to find a way to distribute the data signal and noise in such a way that the resulting binning scheme enables the best temperature estimation, given the characteristics of the data set in question. There are, in fact, only a finite (albeit large) number of ways of binning the input S_X data into output kT bins. The exact number of solutions is 2^n , where $n + 1$ is the number of input S_X bins.⁵ However, there are close to 300 S_X bins in a typical data set of ours, so the number of possible partitions can be close to 2^{300} or 10^{30} , which is intractable to compute one by one. To solve this problem we have developed an algorithm based on ‘dynamic programming’ (see e.g. Cormen et al. 2009, chap. 15), which effectively considers all

⁵ We can think of the problem of partitioning $(n + 1)$ S_X input bins into $(r + 1)$ kT output bins as choosing r amongst the n S_X -bin boundaries as kT -bin boundaries. The number of ways to do so is then $\sum_{r=0}^n {}_n C_r$, where ${}_n C_r = n! / r! / (n - r)!$ are the binomial coefficients appearing on the n -th row of Pascal’s Triangle, whose sum is 2^n .

possible solutions by recursively building up the optimal solution, given some algorithmic criteria.

4.3. Optimal binning algorithm

4.3.1. Fundamentals

We want our temperature profile measurements to have the best-possible distribution of S/N across the full radial range, given the characteristics of the data set in question. Generally, increasing the S/N of one kT bin implies a decrease in the S/N of an adjacent kT bin. Therefore, we will want to maximise the lowest S/N of the temperature profile annuli. Given the steep drop of cluster X-ray emission with radius, the lowest S/N temperature bin is almost always the one farthest from the centre. Conversely, in the centre, where the signal is strong, we prefer to split high-S/N kT bins into more data points having a S/N above some given requirement, rather than accumulating more signal into a single bin. We can formulate the two preferences above algorithmically as follows:

Given two partitions, A and B, of the same S_X -bin range into disjoint kT bins (a.k.a. subsets):

1. The partition whose lowest subset-S/N is higher is preferable. When making this comparison, we cap subset S/Ns at the nominal requirement, thus treating all subsets with S/N above the requirement as equal.
2. If the lowest subset S/N of partitions A and B are identical, the partition whose second-lowest subset-S/N is higher is preferable.
3. This process is continued.
4. If all kT bins of partition A have (capped) S/N matching kT bins in partition B, but B has more kT bins, then B is desirable.

This selection algorithm allows us to systematically decide between any two ways of partitioning a given S_X range of n bins.

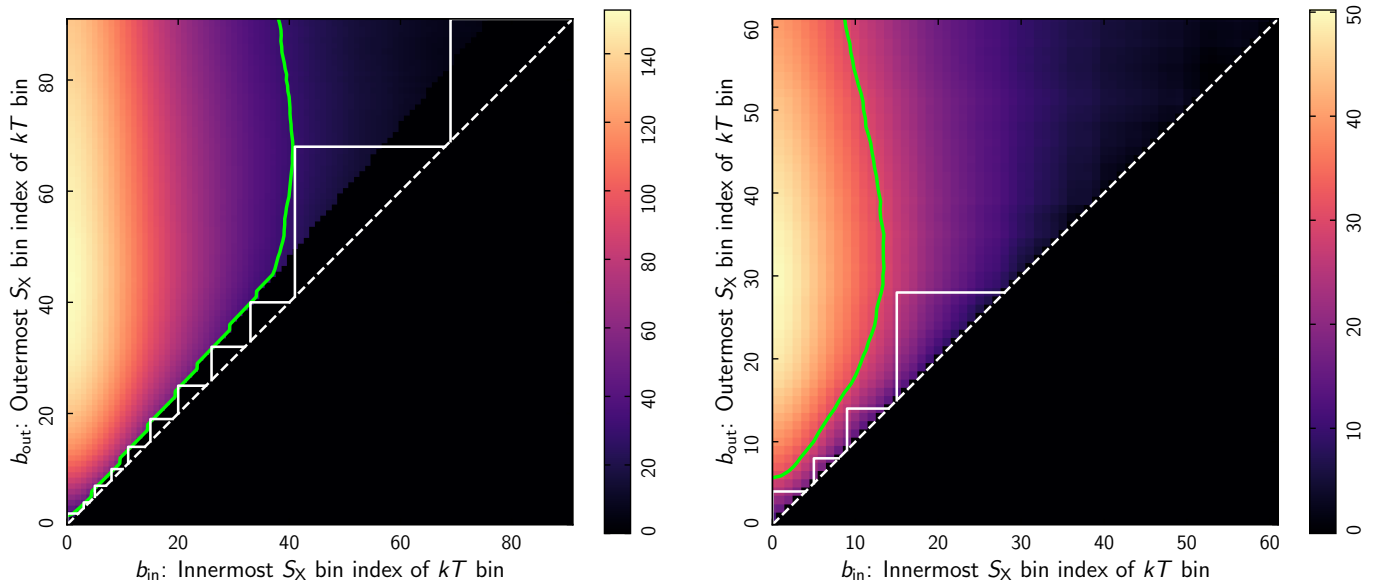


Fig. 7: Two algorithm variations. The S/N landscape is shown here uncapped for illustration, but it is capped in the binning algorithm as described in Sect. 4.3.2. In both panels, the solid curve represents a S/N of 30σ . *Left*: Modified S/N landscape and the resulting binning solution for the galaxy cluster CL0016+16. Here, the output kT bins are required to fulfil four simultaneous criteria: (1) to have a target S/N of 30σ (denoted by the solid curve); (2) to have a minimum S/N $\geq 3\sigma$; (3) to include at least two S_X bins; and (4) to increase in width with a logarithmic factor of 1.2. *Right*: Optimal binning for the low S/N cluster RXJ0030.5+2618, obtained from fixing the number of output kT bins to four and maximising their resulting S/N (see Sect. 4.3.3).

With the technique of dynamic programming, the optimal binning solution for the full S_X -bin range (denoted OP below) is built up recursively from the union of optimal binning solutions for shorter S_X -bin ranges, applying the selection algorithm at every step. If the kT -bin boundaries defined by the optimal binning algorithm are denoted $a, b, c, \dots = 0, 1, 2, \dots, i$, the algorithm is described as follows:

1. We start by considering the trivial one- S_X -bin subranges $[0, 0], [1, 1], [2, 2], \dots$. The only possible (and therefore optimal), binning solution is to have one kT bin containing one S_X bin: $\text{OP}[a, a] = [a, a]$.
2. Then, we solve for two- S_X -bin subranges $[0, 1], [1, 2], [2, 3], \dots$. The two possible solutions are one kT bin containing two S_X bins, $[a, a + 1]$, or two kT bins of one S_X bin each, $[a, a] \cup [a + 1, a + 1]$. We use the selection algorithm described above to decide.
3. We then solve for three- S_X -bin subranges $[a, a + 2]$ as the union of ‘optimal solutions’ for one- S_X -bin and two- S_X -bin subranges that we obtained above: $[a, a] \cup \text{OP}[a + 1, a + 2]$ versus $\text{OP}[a, a + 1] \cup [a + 2, a + 2]$ versus $[a, a + 2]$. Again, we use the selection algorithm to decide. We note that it suffices to consider only unions of two optimal partitions, $\text{OP}[a, i] \cup \text{OP}[i + 1, a + 2]$ for all possible i , and the single partition $[a, a + 2]$ spanning the subrange in consideration. That is to say, we do not need to consider the solution $[a, a] \cup [a + 1, a + 1] \cup [a + 2, a + 2]$ because it is either equivalent to $[a, a] \cup \text{OP}[a + 1, a + 2]$ and to $\text{OP}[a, a + 1] \cup [a + 2, a + 2]$, or it is not an optimal solution.
4. We then solve for four- S_X -bin subranges $[a, a + 3]$ similarly, by comparing unions of two optimal partitions, $\text{OP}[a, i] \cup \text{OP}[i + 1, a + 3]$ for all three possible i , and the single partition $[a, a + 3]$. Again, unions of more than two optimal partitions need not be considered explicitly, as they are either equivalent to some union of two optimal partitions, or are suboptimal.
5. We repeat the previous step to solve for all five- S_X -bin subranges, then six- S_X -bin, ..., until the n - S_X -bin subrange, at

which point we have the optimal binning of the full S_X -bin range.

A key characteristic of our selection algorithm is that for $\text{Partition}[a, b] \cup \text{Partition}[b + 1, c]$ to be $\text{OP}[a, c]$, the two child partitions themselves must be optimal as well.⁶ This ‘optimal substructure’ is what makes dynamic programming applicable to our problem. As seen in the steps above, the recursive build-up of the final solution with dynamic programming involves computing the optimal solution for each subrange only once. These subranges are each present in an exponential number of partitions. Thus, in effect, we are breaking apart the $2^{(n-1)}$ possible partitions of an input of length n and grouping them into $n(n + 1)/2$ subranges, transforming the problem from enumerating and comparing an exponential number of partitions to solving for a polynomial number of subranges. It is therefore possible to cover all $2^{(n-1)}$ possible solutions in polynomial time.

The left-hand panel of Fig. 6 shows this algorithm in action, solving the binning problem in a data-driven manner for the S_X profile of RXJ0856.1+3756 from Fig. 5. In this particular case, the optimal solution requires that the innermost kT bin be larger than some outer ones; a traditional approach such as logarithmic binning is not able to produce such a solution.

It is informative to consider the roles that the partition-selection criteria play:

- At the strong-signal end, the algorithm produces multiple data points by splitting kT bins having S/N above a given threshold. In the left hand panel of Fig. 6, it keeps these data points above, but close to, the line marking the threshold requirement.

⁶ Suppose that $\text{OP}[a, c]$ is $\text{Partition}[a, b] \cup \text{Partition}[b + 1, c]$, but $\text{OP}[a, b]$ is not $\text{Partition}[a, b]$ but rather $\text{Partition}^*[a, b]$. Then $\text{Partition}^*[a, b] \cup \text{Partition}[b + 1, c]$ would give higher S/N than $\text{Partition}[a, b] \cup \text{Partition}[b + 1, c]$, contradicting the initial assertion that the latter is $\text{OP}[a, c]$.

- At the weak-signal end, if our sole criterion were high S/N without splitting kT bins at the strong-signal end, we would always end up with one single kT bin containing all data. This is obviously not helpful in constructing a temperature profile.
- Finally, if we split kT bins having S/N above the threshold at the strong-signal end without simultaneously imposing a S/N maximisation criterion at the weak-signal end, we would end up with the largest-radius kT bin having very low S/N, typically unusable as a temperature-profile data point. This is undesirable because this farthest bin is usually also the widest in a galaxy-cluster X-ray data set; discarding it would mean throwing away a large amount of expensive observational data.

4.3.2. A galaxy-cluster specific amendment

While our algorithm is as generic as possible, it is not specific to typical galaxy cluster X-ray data sets. This means that it still produces suboptimal output, typically yielding outermost kT bins that are too wide. It therefore requires some fine tuning to account for the characteristics of galaxy-cluster X-ray data.

The S/N pattern shown in the centre panel of Fig. 5 is very typical of X-ray observations of galaxy clusters. The S/N decrease with increasing radius is such that when starting from a particular innermost bin b_{in} , it becomes counterproductive to include more S_X bins beyond some radius b_{out} . In the example shown in the left hand panel of Fig. 6, the 30σ contour line reaches a maximum at $b_{in} = 23$, along with a corresponding $b_{out} \approx 48$. In other words, the S/N of a kT bin does not increase monotonically with the bin width. Yet the algorithm deciding between two partitions of the same S_X bin range is agnostic to this peculiar property of galaxy-cluster X-ray data, resulting in the very wide outermost kT bin in the left hand panel of Fig. 6, whose S/N is not as high as it might be.

We thus need to augment the algorithm to prevent it from choosing partitions containing such suboptimal kT bins. In practice, this is achieved by modifying the S/N landscape shown in colour in the left hand panel of Fig. 6 to discourage the algorithm from choosing kT bins that are too wide, that is, those containing extraneous S_X bin(s), the inclusion of which *lowers* the kT -bin S/N, as described in the last paragraph. Because the lowest S/N S_X bins are always at large radii, the algorithm will expand the outermost kT bin inwards as much as possible – sometimes too much – to maximize its S/N in the absence of such S/N landscape modification. Instead, the optimal point to stop expanding inwards can be found by observing that if ‘for a given b_{in} , there is a b_{out} beyond which it is counterproductive to include more S_X bins’, then the corollary is ‘for a given b_{out} , there is an optimal b_{in} beyond which it is not a good use of the overall data to include more S_X bins, despite yielding higher S/N for the kT bin in consideration’.

In the following, we will call this optimal innermost S_X bin to include \tilde{b}_{in} . In practice, we first obtain the optimal outermost S_X bin to include by finding where the S/N reaches its maximum in each b_{in} column, as illustrated by the cyan steps in the left hand panel of Fig. 6. This curve also gives us \tilde{b}_{in} as a function of b_{out} by the corollary above. To prevent the algorithm from moving further inwards, we therefore feed into the algorithm a modified copy of the S/N data, in which the values at $b_{in} < \tilde{b}_{in}$ are capped to the value at \tilde{b}_{in} . This modified S/N landscape is shown in colour in the right hand panel of Fig. 6. Now, the algorithm stops moving further inwards when it reaches \tilde{b}_{in} , and the resulting partitioning scheme (solid white steps) becomes optimal.

Table 3: Variations to the standard binning algorithm applied to each object in our sample. Except for the last four clusters, all binning runs have 30σ scientific S/N goal, minimum 3σ per output kT bin, and minimum two input S_X bins per output kT bin. Clusters with too little data to construct at least four 30σ kT bins have the output kT -bin count fixed to four instead. The profiles for the last four clusters listed at the end of the table are from the analysis of Bartalucci et al. (2019) who used a 20σ criterion. Cols. (1) and (2) ID number and name. Col. (3): Flag whether $4+ 30\sigma$ kT bins is possible. Col. (4): Logarithmic binning factor. Col. (5): Optimised kT -bin count.

ID	Cluster	Flag	Logfac	NT
1	MCXC J0018.5+1626	Y	1.20	11
2	MCXC J0030.5+2618	N	–	4
3	MCXC J0221.1+1958	Y	–	4
4	MCXC J0257.1-2326	Y	1.20	9
5	MCXC J0417.5-1154	Y	1.40	8
6	MCXC J0454.1-0300	Y	1.20	10
7	MCXC J0522.2-3624	N	–	4
8	MCXC J0647.8+7014	Y	0.00	10
10	MCXC J0856.1+3756	Y	–	4
12	MCXC J0943.1+4659	Y	1.20	9
13	MCXC J0957.8+6534	N	–	4
14	MCXC J1003.0+3254	N	–	4
15	MCXC J1120.1+4318	Y	–	4
17	MCXC J1206.2-0848	Y	1.20	13
18	MCXC J1244.0+1653	Y	1.20	7
19	MCXC J1311.5-0551	N	–	4
20	MCXC J1347.5-1144	Y	1.20	12
21	MCXC J1411.4+5212	Y	1.10	6
22	MCXC J1423.7+2404	Y	1.20	8
23	MCXC J1623.5+2634	N	–	4
24	MCXC J1701.3+6414	Y	1.10	7
26	MCXC J2146.0+0423	N	–	4
28	MCXC J2228.6+2036	Y	1.20	11
29	MCXC J2243.3-0935	Y	1.25	11
30	MCXC J2328.8+1453	N	–	4
31	MCXC J2359.5-3211	N	–	4
9	MCXC J0717.5+3745	Y	1.30	10
11	MCXC J0911.1+1746	Y	1.30	9
16	MCXC J1149.5+2224	Y	1.30	6
27	MCXC J2214.9-1400	Y	1.30	8

4.3.3. Algorithm variations

In practice, there are sometimes extra constraints to consider. We encode such constraints as additional modifications to the input S/N landscape, allowing us to run the optimal binning algorithm without change. For example, downstream data processing may require wider kT bins than the input single S_X bins, which translates to the requirement of a minimum input S_X -bin count $N_{in,min}$ per output kT bin. We can implement this by zeroing the S/N values at pixels where $b_{out} - b_{in} < N_{input,min}$ (i.e. those closest to the diagonal). Alternatively, we may want kT bins at least as wide as those one would obtain from logarithmic binning. We can satisfy this constraint by zeroing S/N values where the ratio b_{out}/b_{in} is less than the desired logarithmic binning factor. We can also similarly impose a minimum S/N per output kT bin by zeroing unacceptable pixels in the input S/N landscape. The left hand panel of Figure 7 demonstrates how the algorithm operates when given a number of such constraints.

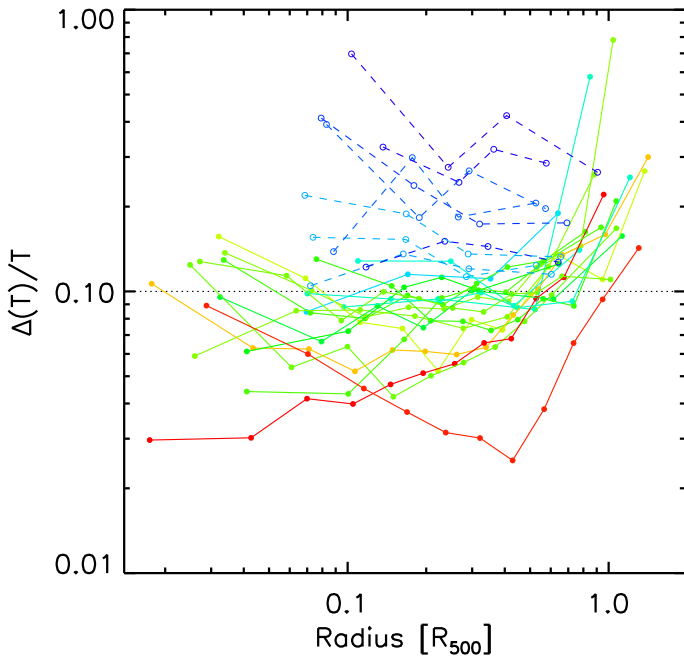


Fig. 8: Relative uncertainty on the temperature as a function of scaled radius, for the profiles defined with 30σ scientific S/N goal (Table 3). The profiles are colour coded as a function of the total S/N in the soft-band (Table 1), from blue (low S/N) to red (high S/N).

Instead of starting from a fixed S/N requirement, we can also fix the number of output kT bins, and let our optimisation algorithm maximise the lowest S/N amongst them. To fix the number of output kT -bin at $N_{\text{out, fixed}}$, we first compute binning solutions to sub-problems of constant numbers of output kT -bin, that is $1, 2, \dots, N_{\text{out, fixed}}$. From these solutions, we build the final fixed-size solution through dynamic programming. This approach tends to be more applicable when the overall S/N is too low to meet an imposed S/N requirement. The right hand panel of Fig. 7 shows an application of this algorithm variation.

4.4. Implementation

For each cluster in our sample, we first produced S_X profiles in the $[0.3, 2.0]$ keV band with data points defined in fixed circular radial bins of $3/3$ width. We ran our optimal binning algorithm with a S/N criterion of 30σ per kT bin, which ensures a $\sim 10\%$ precision on the temperature measurement in each bin. Owing to their faint X-ray emission, some of the objects required a variation to the standard binning algorithm such that a minimum of four optimally binned annuli were produced, as described in Sect. 4.3.3. For high S/N objects, we imposed an additional logarithmic binning factor. We add a criterion that the kT bins are always larger than one S_X bin by imposing that the minimum size of the kT bins be at least two S_X bins wide. Table 3 indicates the variations applied to each cluster. After application of the binning criteria to the S_X profiles, spectra were extracted from each corresponding kT annulus, and fitted as described above.

The temperature profiles of four MACS clusters (ID #9, 11, 16, and 27) listed at the end of Table 3 are from the study of *Planck*-selected clusters by Bartalucci et al. (2019). They used the present optimal binning procedure, but with a S/N criterion of 20σ instead. For consistency with their published work, we kept the original profiles. We also keep their analysis of a

fifth MACS cluster, MCXC J2129.4-0741 (#25), which has a manually-defined four-bin temperature profile.

5. Results

5.1. Optimally binned temperature profiles

The individual temperature profiles are shown in Appendix B. Figure 8 shows the relative uncertainty on the temperature as a function of scaled radius for the full sample, colour-coded by the total soft-band S/N in the R_{500} aperture (i.e. S/N_{500} in Table 1). One can distinguish three regimes. For very high S/N observations (red, orange), the binning out to large radius is driven essentially by the logarithmic binning factor. For observations with an intermediate S/N (yellow, green), the algorithm bins the S_X at 30σ until this is no longer feasible, followed by an additional bin out to R_{500} . The majority of such intermediate S/N clusters therefore display a flat fractional temperature uncertainty with radius, corresponding to $\Delta T/T \sim 10\%$, followed by one single bin with slightly higher fractional uncertainty at the largest scaled radius. Finally, for observations with a low S/N (blue), the algorithm maximises the common S/N for the four-bin minimum criterion; for these objects, the fractional temperature uncertainty is flat with scaled radius, but at a level greater than 10%.

Figure 9 shows the relative precision on each point of the temperature profile as a function of the corresponding S/N in that annular bin. There is a good correlation, justifying a posteriori the underlying assumption of the binning method. There is a dispersion with an apparent increased error with increasing temperature at a given S/N. As the S/N is defined in the soft band this is expected. The upper limit of the band is below the cut-off energy of the bremsstrahlung energy at $E \sim kT$, in most cases. The soft band flux (and thus the S/N in that band) is therefore insensitive to temperature while, with increasing temperature, the energy cut-off moves to higher energy, where the instrument effective area decreases. As this sets the constraints on temperature, its precision also decreases at a given S/N.

Adding information from REXCESS to increase the redshift leverage, we found an empirical power law relation between the relative error, once rescaled as a function of $T/(1+z)$, and the S/N:

$$\frac{\Delta(T)}{T} \times [T_5/(1+z)]^{-0.51} = 0.11 \times \left[\frac{S/N}{30} \right]^{-1.09} \quad (1)$$

where T_5 is the temperature in units of 5 keV. This is illustrated on the right panel of Fig. 9. This relation can be used, for instance, to define the exposure times required to reach a given temperature precision from simple information on the surface brightness profile or the overall count rate.

5.2. Scaled temperature profiles

5.2.1. 3D temperature profiles

The 2D temperature profiles derived using the algorithm described above were deprojected and PSF-corrected as described in Bartalucci et al. (2018). In brief, each individual 2D profile was modelled with a 3D parametric model similar to that proposed by Vikhlinin et al. (2006), convolved with a response matrix that simultaneously takes into account projection and PSF redistribution. The weighting scheme introduced by Vikhlinin (2006) was used to correct for the bias introduced by fitting isothermal models to multi-temperature plasma. Fitting was undertaken with Bayesian maximum likelihood estimation and Markov chain Monte Carlo

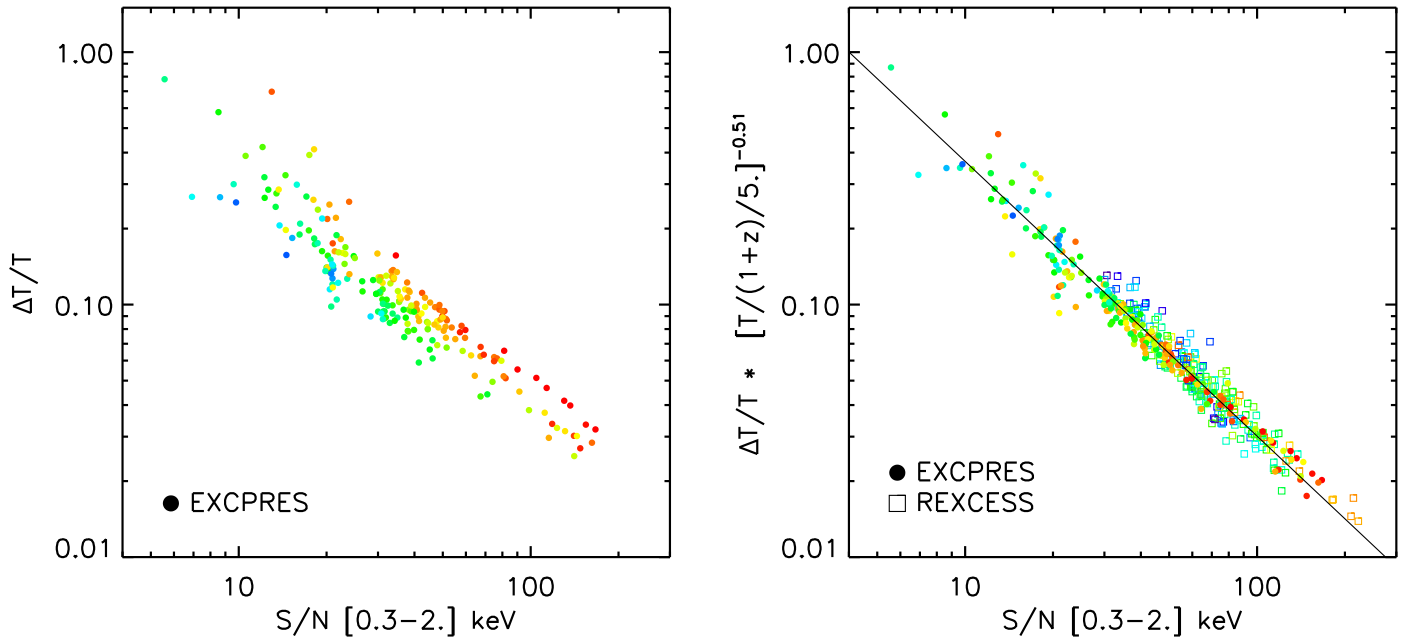


Fig. 9: Relation between S/N and fractional temperature uncertainty. *Left*: Relation between relative error on the temperature and S/N. Each point corresponds to a bin of a temperature profile. *Right*: Rescaled relation, including data from REXCESS at lower redshift. Points are colour coded according to their temperature, lower and higher kT being displayed in blue and red, respectively.

(MCMC) sampling, using `emcee` (Foreman-Mackey et al. 2013). The final deprojected, PSF-corrected profiles were derived from the best-fitting model temperature at the weighted radii corresponding to the 2D annular binning scheme. The left-hand panel of Fig. 10 shows the resulting 3D profiles scaled in terms of R_{500} and T_X , the spectral temperature in the $[0.15 - 0.75] R_{500}$ region, colour-coded as a function of mass. The individual 2D and 3D temperature profiles and associated best fitting models are shown in Appendix B.

5.2.2. Sample average profile

We fitted the scaled profiles $T_m(x) = T(r)/T_X$ with a model consisting of an analytical profile with a radially-varying intrinsic scatter term using the formalism described in Pratt et al. (2022):

$$T_m(x) = f(x) \quad (2)$$

with

$$x = r/R_{500}, \quad (3)$$

with $f(x)$ being described by the model proposed by Vikhlinin et al. (2006)

$$f(x) = T_0 \times \frac{(y + T_{\min}/T_0)}{(y + 1)} \times \frac{(x/x_t)^{-a}}{[1 + (x/x_t)^b]^{c/b}}; \quad y = \left(\frac{x}{x_{\text{cool}}}\right)^{a_{\text{cool}}}. \quad (4)$$

Accounting for measurement errors, the probability of measuring a given scaled gas temperature, T , at given scaled radius, x , is

$$p(T|x) = \mathcal{N}[\log T_m(x), \sigma^2(x)] \quad (5)$$

$$\sigma^2(x) = \sigma_{\text{int}}^2 + \sigma_{\text{stat}}^2 \quad (6)$$

where \mathcal{N} is the log-normal distribution, while the variance, $\sigma^2(x)$, is the quadratic sum of the statistical error σ_{stat} on the measured $\log T(x)$, and of the intrinsic scatter on the median profile

$\log T_m(x)$ at radius x , $\sigma_{\text{int}}(x)$. As in Pratt et al. (2022), we used a non-analytical form for the intrinsic scatter, defining $\sigma_{\text{int}}(x)$ at n equally-spaced points in $\log(x)$ with $\sigma_{\text{int}}(x)$ at other radii being computed by spline interpolation. We used $n = 7$ between $x_{\min} = 0.01$ and $x_{\max} = 1$.

The likelihood of a set of scaled temperature profiles measured for a sample of $i = 1, N_c$ clusters is:

$$\mathcal{L} = \prod_{i=0}^{N_c} \prod_{j=0}^{N_R[i]} p(T_{i,j}|x_{i,j}), \quad (7)$$

where $N_R[i]$ is the number of points of the profile of cluster i , and the quantity $T_{i,j} = T[i, j]/T_{X_i}$ is the scaled temperature measured at each scaled radius $x_{i,j} = r[i, j]/R_{500,i}$, with $T[i, j]$ and $r[i, j]$ being the physical gas temperature and radius. The statistical error on $\log T_{i,j}$ is $\sigma_{\text{stat},i,j}$. We fitted the data (i.e. the set of observed $T[i, j]$) using a Bayesian maximum likelihood estimation with MCMC sampling. Using the `emcee` package developed by Foreman-Mackey et al. (2013), we maximised the log of the likelihood, which is expressed as:

$$\ln \mathcal{L} = -0.5 \sum_{i,j} \left[\ln \sigma_{i,j}^2 + \frac{(\log T_{i,j} - \log T_{m,i,j})^2}{\sigma_{i,j}^2} \right] \quad (8)$$

$$T_{m,i,j} = T_m(x_{i,j}) \quad (9)$$

$$\sigma_{i,j}^2 = \sigma_{\text{int}}^2(x_{i,j}) + \sigma_{\text{stat},i,j}^2. \quad (10)$$

The fit marginalises over a total of fifteen parameters: eight describing the shape of the median profile ($T_{\min}, T_0, x_t, x_{\text{cool}}, a, a_{\text{cool}}, b, c$), and seven additional parameters describing the intrinsic scatter profile. We used flat priors on all parameters.

The orange envelope in Figure 10 shows the resulting best-fitting model overplotted on the EXCPRES data points. The best-

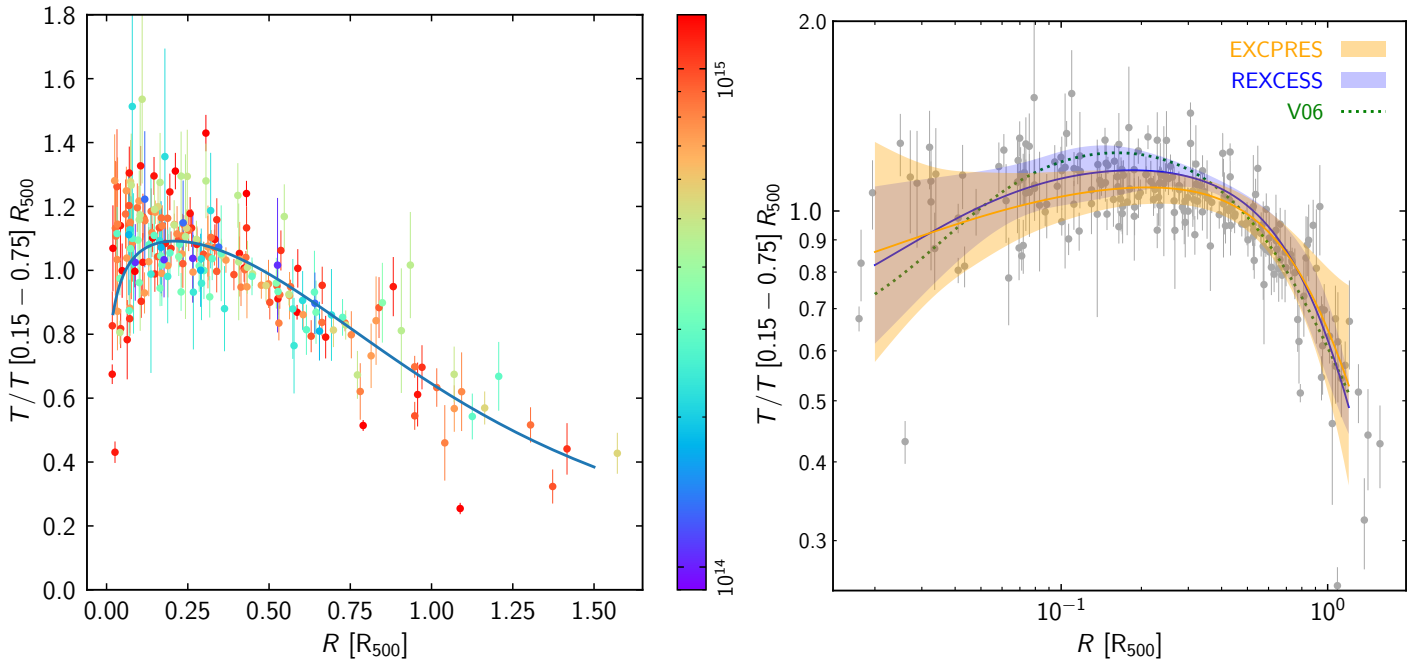


Fig. 10: *Left*: Deconvolved, deprojected, 3D temperature profiles of the EXCPReS sample, scaled by R_{500} and the spectral temperature in the $[0.15 - 0.75] R_{500}$ region, colour-coded by total mass. The best-fitting analytical model (Eqns. 2-5) is overplotted. *Right*: Scaled 3D profiles of the EXCPReS sample (points with error bars) and best-fitting model (orange), compared to the best-fitting model to the scaled temperature profile of the REXCESS sample (blue). Envelopes indicate the radially-varying intrinsic scatter term. The dotted line shows the best-fitting model to the local cool core sample of Vikhlinin et al. (2006).

Table 4: Parameters and marginalised 68% uncertainties of the best-fitting analytical model (Eqns. 2-5), and the natural logarithm of the radial intrinsic scatter term, for the fits to the EXCPReS and REXCESS samples. The fits are illustrated in Fig. 10.

Parameter	EXCPReS	REXCESS
T_{\min}	$0.509^{+0.452}_{-0.452}$	$0.460^{+0.377}_{-0.377}$
T_0	$1.161^{+0.149}_{-0.099}$	$1.160^{+0.097}_{-0.101}$
x	$1.095^{+0.581}_{-0.485}$	$1.261^{+0.391}_{-0.379}$
x_{cool}	$0.039^{+0.185}_{-0.254}$	$0.101^{+0.177}_{-0.155}$
a	$0.036^{+0.070}_{-0.027}$	$0.043^{+0.067}_{-0.033}$
a_{cool}	$0.898^{+0.553}_{-0.378}$	$1.282^{+0.514}_{-0.369}$
b	$2.360^{+0.992}_{-0.533}$	$2.318^{+0.537}_{-0.449}$
c	$2.219^{+1.600}_{-1.145}$	$3.130^{+1.064}_{-1.272}$
σ_1	$0.648^{+0.336}_{-0.348}$	$0.392^{+0.184}_{-0.126}$
σ_2	$0.374^{+0.099}_{-0.081}$	$0.274^{+0.064}_{-0.049}$
σ_3	$0.173^{+0.051}_{-0.040}$	$0.139^{+0.024}_{-0.021}$
σ_4	$0.091^{+0.017}_{-0.014}$	$0.099^{+0.014}_{-0.013}$
σ_5	$0.060^{+0.012}_{-0.012}$	$0.066^{+0.009}_{-0.008}$
σ_6	$0.058^{+0.011}_{-0.011}$	$0.031^{+0.013}_{-0.012}$
σ_7	$0.225^{+0.044}_{-0.033}$	$0.143^{+0.036}_{-0.033}$

fitting parameters for $f(x)$ are as follows:

$$(T_{\min}, T_0, x, x_{\text{cool}}, a, a_{\text{cool}}, b, c) = (0.51, 1.16, 1.09, 0.04, 0.04, 0.90, 2.36, 2.22). \quad (11)$$

The marginalised posterior distributions of each parameter are shown in Fig. C.1. For comparison, we also show in Fig. 10

the best-fitting model obtained from fitting the 3D temperature profiles of the representative local X-ray-selected REXCESS sample (Pratt et al. 2007). Finally, we also overplot the best-fitting model to the local cool-core sample published by Vikhlinin et al. (2006). Outside the central region, the agreement between models is good, suggesting no evolution in the bulk temperature profile within the redshift range probed by the present samples. Agreement in the outer regions is expected from theoretical models of self-similarity. However, within the central $\sim 0.2 R_{500}$ region, there is a suggestion that the cool core sample of Vikhlinin et al. (2006) has a lower central temperature and a higher peak temperature than either of the representative samples. Here, comparison between samples is hampered by radial binning considerations, where cool core systems always have a finer binning than non-cool core systems because of their higher S/N. Further progress on this issue will necessitate careful treatment of the S/N in the central regions, and the inclusion of the dynamical state as an additional parameter (e.g. Bartalucci et al. 2019).

6. Summary and conclusions

In this paper, we introduce EXCPReS, a representative X-ray selected sample of 31 galaxy clusters at moderate redshifts ($0.4 < z < 0.6$), and spanning the full mass range ($10^{14} < M_{500} < 10^{15} M_{\odot}$). EXCPReS was constructed to be an analogue of the low-redshift REXCESS sample (Böhringer et al. 2007).

We used the XMM-Newton observations of the EXCPReS sample to develop and test a new method to produce optimally binned X-ray temperature profiles. The method uses a dynamic programming algorithm based on partitioning of the S_X -bin range to obtain a new binning scheme that fulfils a given S/N threshold criterion out to large radius. Additional optional criteria can be included, including logarithmic radial binning, or setting a minimum number of S_X -bins to be included in each kT -bin. The

method aims at maximising the number of temperature profile bins out to the largest (optionally required) radius. A user-chosen minimum number of bins can be used as a fallback solution for cases with low S/N: in this case, the algorithm maximises the S/N of all bins simultaneously.

We demonstrated the efficiency of our method using the EXCPRs sample, which contains data sets covering a wide range of S/N. The expected correlation between the S/N in kT -bins and the relative error on the temperature shows very little dispersion, but exhibits a clear trend with global temperature. Combining the results from EXCPRs and REXCESS, we derived a relation between the relative uncertainty in kT -bins with respect to the soft-band S_X S/N within these kT -bins, and its dependence on global temperature and redshift (Eq. 1). This relation provides a useful tool for exposure time calculation in X-ray observations, allowing one to obtain an estimate of a given relative error on the ICM temperature measurements, based only on the knowledge of the soft-band number counts.

The optimally binned 2D temperature profiles were PSF-deconvolved and deprojected to derive the 3D profiles. Once scaled by R_{500} and T_X , the temperature in the $[0.15 - 0.75] R_{500}$ region, the 3D EXCPRs temperature profiles exhibit a clear self similar behaviour beyond the core region and increased dispersion towards the centre. We obtained a mean temperature profile for the EXCPRs sample and compared to that from the local X-ray selected REXCESS sample. This comparison shows no obvious sign of evolution in the average temperature profile shape in the redshift range probed in the present study.

In a forthcoming paper we will further investigate the 3D thermodynamic profiles of the EXCPRs sample and how the global properties scale, with respect to the expected self similar evolution and to the cluster mass.

Acknowledgements. Santa, xeus (our local computing facility) for crashing only once during all these years... We would like to thank the people and funding agencies who have supported us over the many years that it has taken us to write this paper. We acknowledge in particular long-term support from CNRS/INSU and from the French Centre National d'Études Spatiales (CNES). The results reported in this article are based on data obtained from the XMM-Newton observatory, an ESA science mission with instruments and contributions directly funded by ESA Member States and NASA.

References

Anokhin, S. G. 2008, *Advances in Space Research*, 42, 576
 Arnaud, M. 2008, in *The X-ray Universe 2008*, 191
 Arnaud, M., Neumann, D. M., Aghanim, N., et al. 2001, *A&A*, 365, L80
 Arnaud, M., Pointecouteau, E., & Pratt, G. W. 2007, *A&A*, 474, L37
 Arnaud, M., Pratt, G. W., Piffaretti, R., et al. 2010, *A&A*, 517, A92
 Art, L. & Mauch, H. 2007, *Dynamic Programming: A Computational Tool, Studies in Computational Intelligence* (Springer Berlin, Heidelberg)
 Baldi, A., Ettori, S., Mazzotta, P., Tozzi, P., & Borgani, S. 2007, *ApJ*, 666, 835
 Baldi, A., Ettori, S., Molendi, S., & Gastaldello, F. 2012, *A&A*, 545, A41
 Bartalucci, I., Arnaud, M., Pratt, G. W., Démoclès, J., & Lovisari, L. 2019, *A&A*, 628, A86
 Bartalucci, I., Arnaud, M., Pratt, G. W., et al. 2017, *A&A*, 598, A61
 Bartalucci, I., Arnaud, M., Pratt, G. W., & Le Brun, A. M. C. 2018, *A&A*, 617, A64
 Bleem, L. E., Stalder, B., de Haan, T., et al. 2015, *ApJS*, 216, 27
 Böhringer, H., Schuecker, P., Guzzo, L., et al. 2004, *A&A*, 425, 367
 Böhringer, H., Schuecker, P., Pratt, G. W., et al. 2007, *A&A*, 469, 363
 Böhringer, H., Voges, W., Huchra, J. P., et al. 2000, *ApJS*, 129, 435
 Burenin, R. A., Vikhlinin, A., Hornstrup, A., et al. 2007, *ApJS*, 172, 561
 Burke, D. J., Collins, C. A., Sharples, R. M., Romer, A. K., & Nichol, R. C. 2003, *MNRAS*, 341, 1093
 Cormen, T. H., Leiserson, C. E., Rivest, R. L., & Stein, C. 2009, *Introduction to Algorithms* (MIT Press and McGraw-Hill)
 Croston, J. H., Arnaud, M., Pointecouteau, E., & Pratt, G. W. 2006, *A&A*, 459, 1007
 De Grandi, S. & Molendi, S. 2002, *ApJ*, 567, 163

Ebeling, H., Barrett, E., Donovan, D., et al. 2007, *ApJ*, 661, L33
 Ebeling, H., Edge, A. C., Mantz, A., et al. 2010, *MNRAS*, 407, 83
 Foreman-Mackey, D., Hogg, D. W., Lang, D., & Goodman, J. 2013, *PASP*, 125, 306
 Gioia, I. M., Maccararo, T., Schild, R. E., et al. 1990, *ApJS*, 72, 567
 Hasselfield, M., Hilton, M., Marriage, T. A., et al. 2013, *J. Cosmology Astropart. Phys.*, 2013, 008
 Henry, J. P. 2004, *ApJ*, 609, 603
 Henry, J. P., Mullis, C. R., Voges, W., et al. 2006, *ApJS*, 162, 304
 Horner, D. J., Perlman, E. S., Ebeling, H., et al. 2008, *ApJS*, 176, 374
 Kalberla, P. M. W., Burton, W. B., Hartmann, D., et al. 2005, *A&A*, 440, 775
 Kay, S. T. & Pratt, G. W. 2022, in *Handbook of X-ray and Gamma-ray Astrophysics*. Edited by Cosimo Bambi and Andrea Santangelo, 100
 Kotov, O. & Vikhlinin, A. 2005, *ApJ*, 633, 781
 Kravtsov, A. V. & Borgani, S. 2012, *ARA&A*, 50, 353
 Kravtsov, A. V., Vikhlinin, A., & Nagai, D. 2006, *ApJ*, 650, 128
 Leccardi, A. & Molendi, S. 2008, *A&A*, 486, 359
 Lovisari, L. & Maughan, B. J. 2022, in *Handbook of X-ray and Gamma-ray Astrophysics*. Edited by Cosimo Bambi and Andrea Santangelo, 65
 Lovisari, L., Reiprich, T. H., & Schellenberger, G. 2015, *A&A*, 573, A118
 Lumb, D. H., Bartlett, J. G., Romer, A. K., et al. 2004, *A&A*, 420, 853
 Mann, A. W. & Ebeling, H. 2012, *MNRAS*, 420, 2120
 Mantz, A. B., Allen, S. W., Morris, R. G., & Schmidt, R. W. 2016, *MNRAS*, 456, 4020
 Markevitch, M. 1998, *ApJ*, 504, 27
 McDonald, M., Benson, B. A., Vikhlinin, A., et al. 2014, *ApJ*, 794, 67
 Melin, J. B., Bartlett, J. G., & Delabrouille, J. 2006, *A&A*, 459, 341
 Mullis, C. R., McNamara, B. R., Quintana, H., et al. 2003, *ApJ*, 594, 154
 Perlman, E. S., Horner, D. J., Jones, L. R., et al. 2002, *ApJS*, 140, 265
 Piffaretti, R., Arnaud, M., Pratt, G. W., Pointecouteau, E., & Melin, J.-B. 2011, *A&A*, 534, A109
 Planck Collaboration VIII. 2011, *A&A*, 536, A8
 Planck Collaboration XXIX. 2014, *A&A*, 571, A29
 Planck Collaboration XXVII. 2016, *A&A*, 594, A27
 Pratt, G. W. & Arnaud, M. 2003, *A&A*, 408, 1
 Pratt, G. W., Arnaud, M., Maughan, B. J., & Melin, J. B. 2022, *A&A*, 665, A24
 Pratt, G. W., Arnaud, M., Piffaretti, R., et al. 2010, *A&A*, 511, A85+
 Pratt, G. W., Böhringer, H., Croston, J. H., et al. 2007, *A&A*, 461, 71
 Repp, A. & Ebeling, H. 2018, *MNRAS*, 479, 844
 Romer, A. K., Nichol, R. C., Holden, B. P., et al. 2000, *ApJS*, 126, 209
 Rykoff, E. S., Rozo, E., Hollowood, D., et al. 2016, *ApJS*, 224, 1
 Sadibekova, T., Arnaud, M., Pratt, G. W., Melin, J., & P. Tarrío, P. 2023, *A&A*
 Sadibekova, T., Arnaud, M., Pratt, G. W., Tarrío, P., & Melin, J. B. 2024, *arXiv e-prints*, arXiv:2402.01538
 Schaye, J., Crain, R. A., Bower, R. G., et al. 2015, *MNRAS*, 446, 521
 Schaye, J., Kugel, R., Schaller, M., et al. 2023, *arXiv e-prints*, arXiv:2306.04024
 Sun, M., Voit, G. M., Donahue, M., et al. 2009, *ApJ*, 693, 1142
 Ulmer, M. P., Adami, C., Covone, G., et al. 2005, *ApJ*, 624, 124
 Vikhlinin, A. 2006, *ApJ*, 640, 710
 Vikhlinin, A., Kravtsov, A., Forman, W., et al. 2006, *ApJ*, 640, 691
 Vikhlinin, A., Markevitch, M., Murray, S. S., et al. 2005, *ApJ*, 628, 655
 Vikhlinin, A., McNamara, B. R., Forman, W., et al. 1998, *ApJ*, 502, 558
 Vogelsberger, M., Genel, S., Springel, V., et al. 2014, *MNRAS*, 444, 1518
 Wen, Z. L. & Han, J. L. 2015, *ApJ*, 807, 178

Appendix A: Clusters with XMM-Newton observations not included in EXCPRoS

The MCXC clusters in the low-luminosity sample ($L_{500} < 4 \times 10^{44}$ ergs s^{-1}) with archival observations, but not included in the EXCPRoS sample, are listed in Tab. A.1. The table also gives the OBSID of the XMM-Newton observation and the reference of relevant published XMM-Newton analysis. We further analysed the archival data of some of the clusters.

MCXC J1002.6-0808 was observed in the framework of our Large Programme #030258. The observation revealed that MCXC J1002.6-0808 is a point source, which is also confirmed by the *Chandra* image.

Our study of the image of MCXC J1419.8+0634 shows that it is a bimodal cluster, thus not suitable for radial analysis.

We require a minimal S/N ratio of $S/N = 20$, needed to derive a temperature profile as shown by our work. The other clusters could not be retained because the archival observations are not deep enough:

- The observations of the two EMSS clusters, MCXC J0305.3+1728 ($z = 0.425$) and MCXC J2056.3-0437 ($z = 0.583$), are shallow, with clean observing time of ~ 10 ksec and 12 ksec, respectively (Baldi et al. 2012, their Tab.1). The error on the global temperature is $\pm 15\%$. Baldi et al. (2012) were only able to extract the temperature in 2 bins up to $0.4R_{500}$ for MCXC J2056.3-0437.
- The observations of MCXC J1325.5-3825, MCXC J0505.3-2849, MCXC J1354.2-0221, MCXC J0847.1+3449 and MCXC J0337.7-2522 were early follow up of SHARC clusters to meant to measure a global temperature and the luminosity, published by Lumb et al. (2004). Our full re-analysis of MCXC J0505.3-2849, the best measured cluster of the list, gives a $S/N_{500} = 20$. The observations of the other clusters are at lower S/N, taking into account the precision on the observed flux (their table 5). MCXC J1325.5-3825 falls in the field of view of an observation centered on IRAS 13224–3809, a very bright Seyfert galaxy. Many more observations have become available over the years, but only in Window mode, and centred on the galaxy.
Note that the two other clusters of their sample at $0.4 < z < 0.6$, MCXC J1120.1+4318 and MCXC J1701.3+6414 (re-observed by XMM-Newton), are included in the EXCPRoS sample.
- Together with MCXC J0337.7-2522 studied by Lumb et al. (2004), MCXC J2202.7-1902 and MCXC J0858.4+1357 are the three $0.4 < z < 0.6$ clusters with the lowest luminosities, $L_{500} < 10^{44}$ ergs/s, observed by XMM-Newton. Anokhin (2008) gives a temperature of about 3 keV for MCXC J2202.7-1902 and MCXC J0858.4+1357. From our analysis of the surface brightness profiles and global properties, we derived a S/N ratio of $S/N=15$ and $S/N_{500}=19$, respectively. This entails that the EXCPRoS selection could not be extended below $L_{500} = 10^{44}$ ergs/s.
- MCXC J0056.9-2740 ($z = 0.56$) falls in the field of the programme ‘A shallow XMM survey of AAT 2DF fields SSC_32’ (PI M. Watson). This includes two short observations of 7.2 ksec (highly flared) and 8.9 ksec, respectively. This is too shallow to obtain spatially resolved spectroscopy of the $z = 0.56$ cluster and indeed the examination of the EPIC image shows that the cluster is poorly detected. MCXC J0056.9-2740 coincides with the source 4XMM J005657.1-274028, detected at 13σ in the 4XMM-DR13 catalogue.
- MCXC J1205.8+4429 is a fossil group, as shown by Ulmer et al. (2005). From their Table 2, the S/N of the group obser-

vation is $S/N \sim 21$ and there is a $\pm 10\%$ error on the global temperature.

In conclusion, the final selection for the low luminosity box of EXCPRoS includes clusters with $0.44 < z < 0.56$ and $10^{44} < L_{500} < 4 \times 10^{44}$ ergs s^{-1} . Four further objects with archival data fall in that range but are not retained: three SHARC clusters published by Lumb et al. (2004) since the exposure is not deep enough, and a 160SD/WARPS object which is false detection.

Appendix B: Individual temperature profiles

Individual temperature profiles of the EXCPRoS sample are shown in Fig. B.1 and B.2. In all panels, the black points with error bars show the annular temperature measurements. Solid green lines show the best fitting 3D temperature model, with its uncertainty indicated by the dashed green lines. Red lines show the 2D reprojection of the best fitting 3D model, and dashed red lines the associated uncertainty.

Appendix C: Posteriors

Marginalised posterior likelihood for the parameters of the best-fitting temperature profile model to the EXCPRoS data, as detailed in Sect. 5.2.

Table A.1: Clusters in the $0.4 < z < 0.6$ range with XMM-Newton archival data but not included in the EXCPReS sample. The clusters are ordered by increasing redshift. Columns are 1-2: Cluster MCXC name and other name, 3: Detection survey, 4: Redshift, 5: XMM-Newton OBSID, 6: Reference to relevant publication or present work; (1) Baldi et al. (2012); (2) Anokhin (2008); (3) Lumb et al. (2004); and (4) Ulmer et al. (2005)

Name	Other Name	Catalogue	z	OBSID	Ref
MCXC J0305.3+1728	MS0302.5+1717	EMSS	0.425	0112190101	1
MCXC J2202.7-1902	RX J2202.7-1902	160SD, S-SHARC, WARPSII	0.438	0203450201	2, pw
MCXC J1325.5-3825	RX J1325.5-3826	S-SHARC	0.445	0110890101	3
MCXC J0858.4+1357	RX J0858.4+1357	160SD, S-SHARC, WARPSII	0.488	0203450101	2, pw
MCXC J0505.3-2849	RX J0505.3-2849	S-SHARC	0.509	0111160201	3, pw
MCXC J1002.6-0808	RX J1002.6-0808	160SD, WARPSII	0.524	0302580301	pw
MCXC J1354.2-0221	BVH2007 181	400SD, S-SHARC, 160SD	0.546	0112250101	3
MCXC J0847.1+3449	RX J0847.1+3449	160SD	0.560	0107860501	3
MCXC J0056.9-2740	RX J0056.9-2740	160SD	0.563	0111280201	pw
				0111282001	
MCXC J1419.8+0634	WARP J1419.9+0634	WARPSII, 160SD	0.564	0303670101	1, pw
MCXC J2056.3-0437	MS2053.7-0449	EMSS	0.583	0112190601	1
MCXC J0337.7-2522	RX J0337.7-2522	160SD, S-SHARC	0.585	0107860401	3
MCXC J1205.8+4429	WARP J1205.8+4429	WARPSII	0.592	0156360101	4

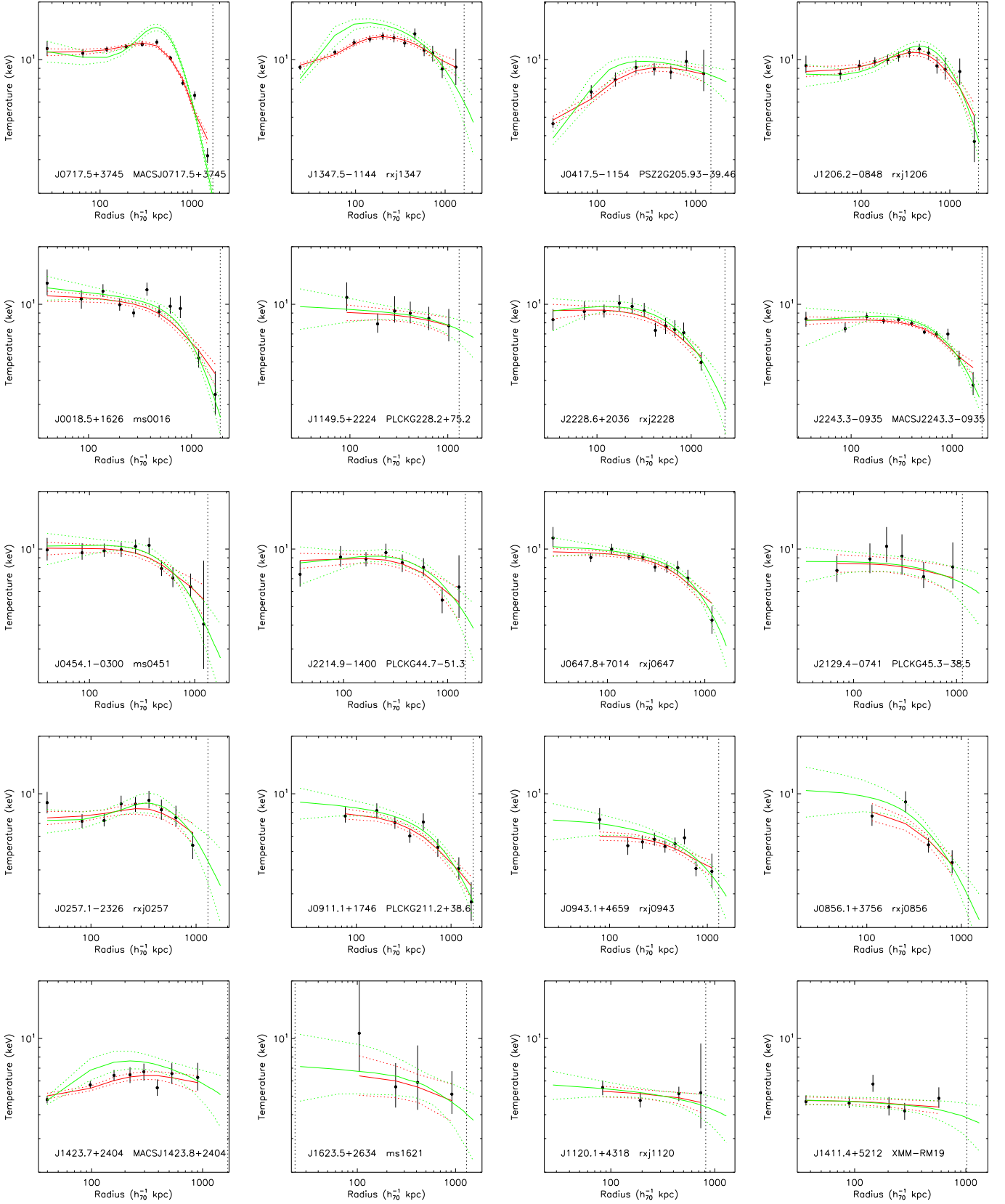


Fig. B.1: Individual temperature profiles of the EXCPRoS sample. Black points with error bars show the annular temperature measurements. Green lines show the best fitting 3D temperature model. Red lines show the 2D reprojected of the best fitting 3D model. The model uncertainties are indicated by dashed lines.

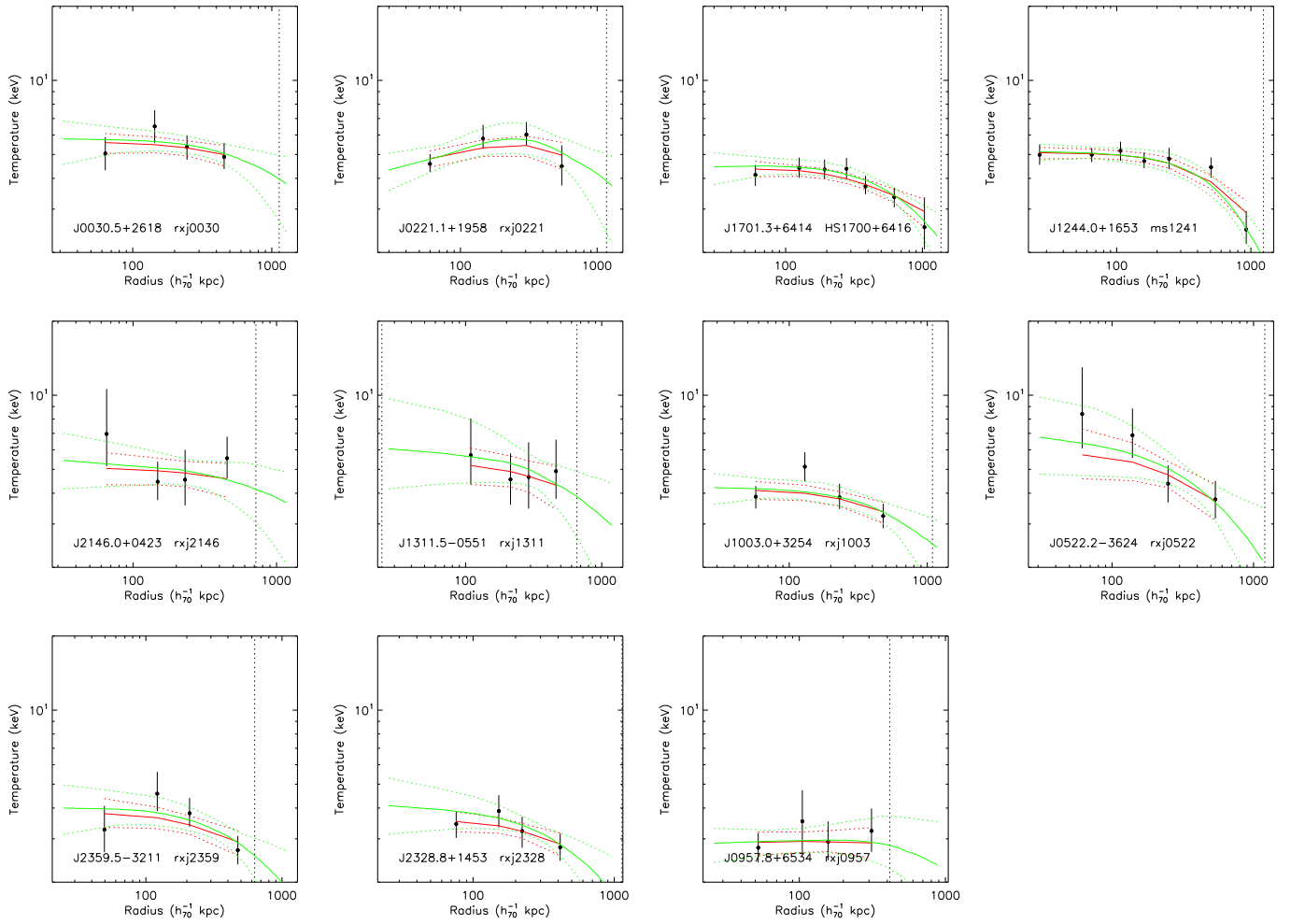


Fig. B.2: continued

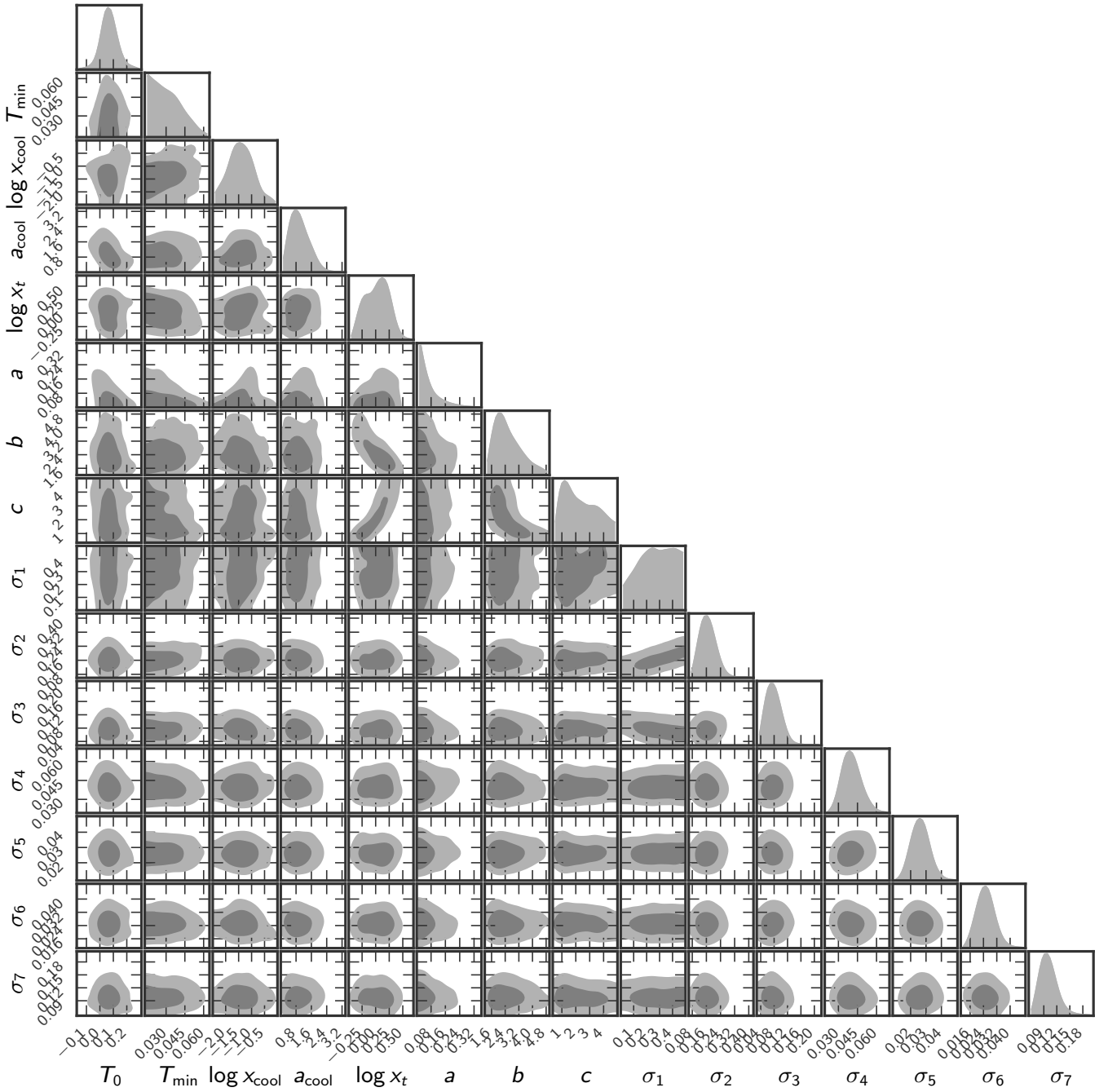


Fig. C.1: Marginalised posterior likelihood for the parameters of the best-fitting temperature profile model to the EXCPRoS data.